Journal of Intelligent & Robotic Systems (2022) 106:61
https://doi.org/10.1007/s10846-022-01757-3

REGULAR PAPER

Stewart-Inspired Vibration Isolation Control for a Wheel-legged Robot via Variable Target Force Impedance Control

Junfeng Xue[1] · Shoukun Wang[1] · Junzheng Wang[1] · Zhihua Chen[1,2]

Received: 12 June 2022 / Accepted: 7 October 2022 / Published online: 10 November 2022

Abstract
The vibration isolation control for wheel-legged robot has been widely investigated when adapting to the undulating slope terrain. How to solve the lag problem of low accuracy of foot-end force convergence to fixed target force in traditional impedance control under continuously changing slope terrain is the main challenge. In this paper, a vibration isolation control strategy based on variable target force impedance control (VTFIC) is proposed to effectively realize the foot-end contact force to track the target force under uneven road while maintaining the stability of the body. The strategy includes foot-end disturbance force estimator (FDFE) and force convergence accelerating controller (FCAC). Firstly, FDFE includes slope angle model, slope terrain model, autoregressive comprehensive moving average (ARIMA) model and event-triggering mechanism. It is mainly used to predict and calculate the disturbance force of slope terrain, and solve the problem of high deviation between foot-end actual force and target force caused by the impulse when foot contact with slope. Secondly, FCAC is designed based on power functional feed-forward control, to accelerate the convergence speed of the foot-end contact force to the target force. Finally, the simulation and experiment results show that the foot-end contact force of the robot can effectively track the target force with high accuracy and the robot remains stable under various terrains.

Keywords Wheel-legged robot · Vibration isolation control · Variable target force impedance control · Impedance control · Kinetic analysis

1 Introduction

Wheel-legged robot combines the excellent mobility of the legged robot on the rough ground and the ability to move quickly and save energy of the wheeled robot on the flat ground [1–12]. Thus, it has become the research object of many research institutions. For example, a leg-wheel hybrid mobile robot was proposed in [13], which can walk in legged mode or make wheeled locomotion by roller-skating using the passive wheels. In [14], the wheel-leg hybrid robot have great ability passing uneven road. Benefits from its structure, the robot can climb over the obstacle much higher than its wheel radius. Moreover, the wheel and leg can transform to each other in robot from [15], which can also realize a greater ability to climb obstacles. In [16], a general system for the four wheel-leg robot was developed, which can negotiate the obstacle by its hip joint and knee joint to adapt to the uneven terrain with high stability. In [17], a novel hydraulic wheel-legged robot (WLR) combined with a humanoid structural design was developed. Besides, compared with series mechanism, parallel mechanism robot can make up for the weak resistance of driving parts to disturbance in the process during motion. Consequently, the wheel-legged robot with parallel leg structure has also attracted attention. In [18, 19], a parallel mechanism wheel-legged robot named BIT-NAZA was proposed, which can realize foot stable walking. In [20], a hexapod robot with parallel legs named Octopus was proposed, which can be used in nuclear disaster rescue missions.

Meanwhile, vibration isolation control is the key factor to realize the wheeled stable driving of the body for wheel-legged robot, and its performance plays an important role in practical engineering [21]. At the moment, the research

✉ Zhihua Chen
zhihua.chen@nchu.edu.cn

[1] State Key Laboratory of Complex System Intelligent Control and Decision, School of Automation, Beijing Institute of Technology, 100081 Beijing, China

[2] MOE Key Lab of Nondestructive Testing Technology, School of Information Engineering, Nanchang Hangkong University, 330063 Nanchang, China

of vibration isolation control mainly focuses on the development of traditional impedance control-based compliance controller [22], whole-body controller based on posture control, and adaptive variable impedance controller [23]. For instance, a cooperative control framework for wheel-legged robot was proposed in [24, 25], including impedance controller, attitude controller and barycenter height controller. The impedance controller is used to solve the vibration isolation and suspension problems of the robot. In [26], a whole-body dynamic model about two wheel-leg robot was built, which can control the speed, height and angle for torso precisely without force sensor. In addition, an whole-torso control strategy based on foot force distribution and attitude control was proposed in [10, 27], which can be used to control multi degree of freedom legs to perform high flexible motion and adapt to rough terrain.

Generally speaking, adaptive impedance is divided into indirect adaptive control based on position compensation and adaptive impedance control based on variable impedance parameters [28]. Considering the uncertainty of the environment, the vibration isolation control method based on adaptive variable impedance control can be used to improve the motion ability of the robot under unknown conditions. At present, it is also an extensive research direction. For example, an adaptive impedance controller for human-robot co-transportation was proposed in [29–31], which realizes the safe interaction and smooth control behavior between human-robot. In [32], a nonlinear model adaptive reference controller was proposed to estimate the reference trajectory in the impedance model, which provides the desired stable impedance control effect for the robot end effector. Meanwhile, a new adaptive variable resistance tracking control method was proposed in [33], which can track the dynamic expected force by adaptively changing the damping parameters. In [34], an adaptive variable impedance control (AVIC) method was proposed to minimize the force-tracking error for the forces of each leg, which may improve the stability of the horizontal of robot body.

Besides, considering the uncertainty of environment, the consideration of kinetic analysis can be of great importance to enhance the capability of robot moving in unknown condition. In [35], a modular framework was proposed to generate robust biped motion by using the close coupling between analytical walking method and deep reinforcement learning. A reactive controller combined with RL can incorporate intricate information including terrain and vehicle dynamics [36]. This controller enhances the mobility of finding effective exit way in instable situation. In [37], the integral reinforcement learning (IRL) has been proposed to solve the problem of little information of the human arm model to minimize the motion tracking error. In the past three years, with the increasing complexity of robot working environment, more and more researchers have studied the dynamics of impedance control in the nonlinear field. In [38], the Szász–Mirakyon operator approximating the unmodeled dynamic model and the uncertain factors including external disturbances are proposed. In order to make the robot follow the specified motion accurately, an impedance control algorithm is designed to transfer the user's input force and human upper limb stiffness to the impedance model in [39]. The paper [40] presents Model-Based Reinforcement Learning (MBRL) variable impedance controller. By learning the human-computer interaction dynamic model and optimizing the stiffness and damping parameters linearly, the operator and the manipulator can complete the collaborative task.

In the previous work, in order to improve the smoothness of wheel-legged robot in uneven terrain, a distributed active disturbance rejection control framework and a speed consistency strategy based on consistency algorithm were proposed in [41]. An improved sliding mode variable structure robust controller was proposed in [42] to improve the high-precision control of position inner loop. In [43], an observer-based robust controller equipped with a fast friction estimator was proposed for a 6-DOF parallel electrical manipulator (PEM) in the joint-task space. However, how to apply the adaptive vibration isolation control based on variable target force to the wheel-legged robot to realize the stable driving of the robot in unstructured terrain is still the main challenge, especially in continuously changing slope terrain. Thus, a vibration isolation control strategy based on VTFIC for the developed robot in this paper. The main contributions are listed as follows:

1. In order to realize the stable vibration isolation of the body when the robot wheels over continuous slope terrain, a novel a vibration isolation control strategy based on VTFIC is proposed, including FDFE and FCAC.
2. FDFE is established to predict and calculate the disturbance force of slope terrain. We deduce slope angle model, slope terrain model, and take use of ARIMA model, event-triggering mechanism to realize this modular to reduce the dynamic force error of foot-end. Especially, we creatively discretize the robot speed to solve the above model. FCAC is a feed-forward controller with power function, to accelerate the convergence speed of the foot-end contact force to target force.
3. Associated experiments demonstrate that the developed vibration isolation control strategy based on VTFIC has adequate performance for the engineering applications when the robot wheels over continuous slope terrain.

The whole content of the article is distributed as follows. Section 2 introduces the contact model between the foot-end and the terrain of the robot and the lag problem of the force tracking control of the traditional impedance. Section 3 introduces the theoretical basis and framework of the

adaptive impedance control strategy with variable target force (VTFIC). The stability of VTFIC is proved in this section. Simulation and experiment results in Section 4 verify the adaptive impedance control strategy with variable target force. Eventually, in Section 5, we summarize the experimental results and look forward to the future work.

2 Wheel-leg Robot and Limitations of Traditional Impedance Control

2.1 BIT-NAZA-II

The six wheel-legged robot, BIT-NAZA-II, in this study is an electric parallel structure robot. The characteristic of the robot is that each leg is composed of an inverted Stewart platform. The wheels are installed on the upper part of the Stewart platform. The electric cylinder and wheel motor in the Stewart platform are the core driving devices of the system. The parallel wheel leg structure of the robot can make the robot do more flexible, diverse and stable movements. The goal of robot is to carry out transportation or rescue tasks with high stability in unknown complex environment. The main parameters of BIT-NAZA-II are listed in Table 1.

BIT-NAZA-II is composed of four parts: environment perception system, computer control system, energy system and leg actuator system. The robot and its structure are shown in Fig. 1.

1. Environment perception system: It consists of differential GPS (Global Positioning System), lidar, CCD (Charge Coupled Device) camera, infrared camera and two-dimensional turntable. These sensors can obtain the GPS coordinates, orientation, depth information of surrounding obstacles and image information of the robot. The two-dimensional turntable can change the orientation of the CCD camera, so that the robot can obtain image information at a larger angle.
2. Control system: Composed of embedded computers, master computer and environment aware computer. The six embedded computers can interact with the actuators of each leg through the CAN (Controller Area Network) bus to control each electric actuator to perform the specified motion. At the same time, the master computer can exchange information with the embedded computers and environment aware computer through router UDP (User Datagram Protocol). The master computer is responsible for coordinating the work of each embedded computer, planning and controlling the movement of the robot actuator. The environment sensing computer can collect and process the image lidar data.
3. Energy system: It includes motion power battery, control system power battery and battery management system. The motion power battery provides power for 36 electric cylinders and 6 motors of the robot. The control system power battery provides power for various computers. Battery management system can obtain information of batteries and control the charge of it.
4. Leg actuator system: It is composed of 36 electric cylinders and 6 motors. Each leg is composed of an inverted Stewart platform. The platform actuator is composed of 6 electric cylinders. In order to reduce the weight of the foot-end, the motor located in the fuselage drives the wheels located at the foot end through the universal shaft.

Table 1 The main parameters of the robot

Item	Values	Units
Weight	400	kg
Maximum Load Capacity	350	kg
Length	1.8	m
Width	1.8	m
Height	1.4	m
Maximum Legged speed	1.2	m/s
Maximum Wheeled speed	20	km/h
Battery Time	5	h
Motion Mode	3	

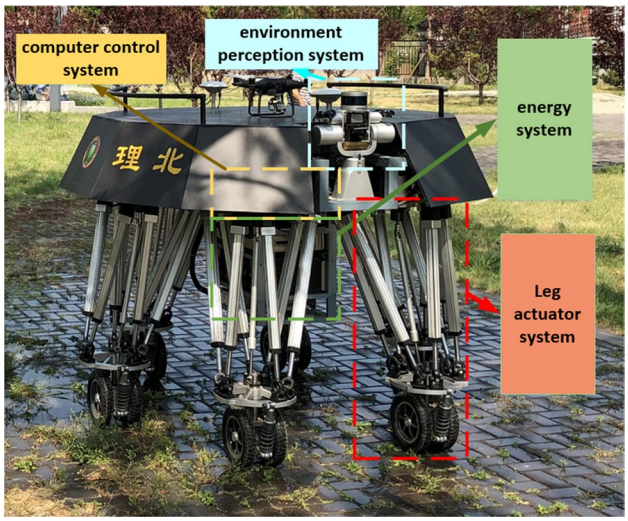

Fig. 1 BIT-NAZA-II

The vibration isolation control of the wheeled robot can realize the stable and fast movement of the robot. Among them, impedance control (IC) is a very important research content. In the next subsections, we introduce the mechanism of IC and the theoretical analysis of its large force error during the process of dynamic motion on uneven terrain.

2.2 Equivalent Contact Model Between Foot-end and Terrain

In this section, we establish the equivalent contact model between the foot-end of the leg and the terrain for the problem of vibration isolation control in the Z-direction when the robot wheels pass through the slope, as shown in Fig. 2.

In Fig. 2, $X_BY_BZ_B$ is the inertial coordinate system. M^d, B^d and K^d represent the target mass, target stiffness and target damping of the single leg impedance control based on velocity of the robot respectively. L_{leg} and L_{wheel} represent the leg length and wheel diameter when the electric cylinders of the leg are half extended. P_t, X_t^a, X_t^e respectively represent the contact point between foot-end and ground, actual position of foot-end, and terrain position in the Z-direction when the robot passes the slope at time t. X_t^c, the output of IC, is the target length of each leg. When the Stewart platform control method is an error free controller and has stabilized, X_t^c equals to X_t^a theoretically. θ_t is the angle between the tangent passing through contact point P_t and the horizontal plane at time t. Thus, in order to realize the vibration isolation control of the robot leg, the robot needs to adjust the position of its leg actuator in the Z-direction through the IC algorithm to track the foot-end target force in the Z-direction. The impedance control based on velocity can be described as follows

$$M^d(\ddot{X}^a - \ddot{X}^d) + B^d(\dot{X}^a - \dot{X}^d) + K^d(\dot{X}^c - \dot{X}^d) = F^e - F^d \quad (1)$$

where X^d, F^d and F^e represent the desired position, target tracking force and the contact force between the foot-end and the terrain in the Z-direction, respectively.

In addition, we use the spring damping system to build the contact model between the foot-end and the ground. The contact model is as follows

$$F^e = \begin{cases} m^e(\ddot{X}^e - \ddot{X}^a) + b^e(\dot{X}^e - \dot{X}^a) + k^e(X^e - X^a), & X^e > X^a \\ 0, & X^e \le X^a \end{cases} \quad (2)$$

where k^e, b^e are the stiffness and target damping of the terrain respectively. m^e is the mass of robot per-leg.

2.3 The Theoretically Defect of Traditional Impedance Control

As shown in Fig. 3, in this section, we analyze the changes of force of robot when it passes through slope terrain with or without impedance control. Green and black dotted line represent F^{dis} and F^d respectively. F^e and F^E respectively represent foot-end contact force with and without impedance control (blue dotted line and red curve).

When the robot's leg passes through the slope terrain, we assume that the actual position X^a of the foot-end almost coincides with the environmental position X^e (pink curve in Fig. 3) due to the terrain and foot-end shape variables cannot be observed by naked eye. In Fig. 3, F^{dis} at the contact points P_1, P_2 and P_3 between the foot-end and the slope at time T_1, T_2 and T_3 are different. And F^{dis} is affected by the impulse of the contact between foot-end and slope. The value of disturbance force F_t^{dis} gets positive correlation with angle θ_t. Therefore, the calculation formula of F^e with or without IC is as follows

$$\begin{cases} F_{t+1}^e = F_t^e + F_t^{dis} + F_t^I \to F^d, & \text{with impedance} \\ F_{t+1}^E = F_t^E + F_t^{dis}, & \text{without impedance} \end{cases} \quad (3)$$

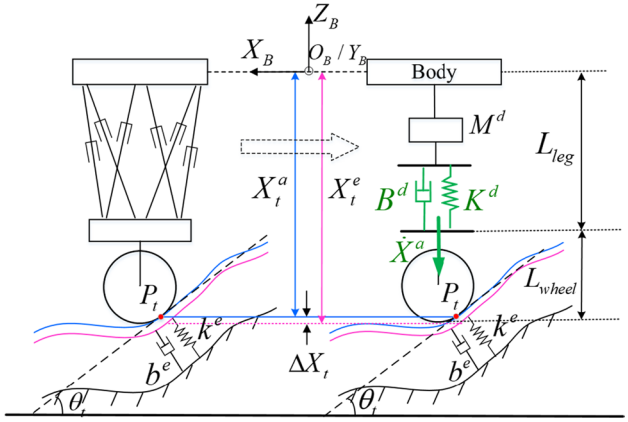

Fig. 2 The equivalent contact model between the foot-end of the leg and the terrain

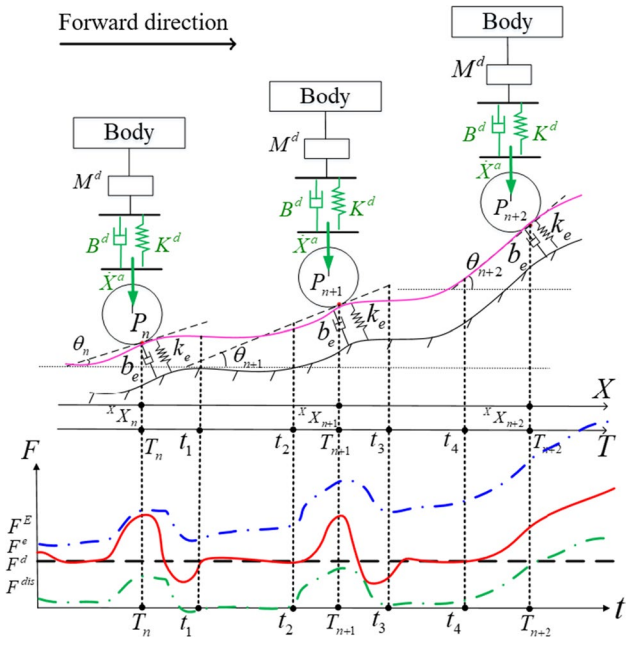

Fig. 3 The curves of foot-end contact force, disturbance force and target force of robot's leg passing through slope terrain with or without impedance control

where F_t^I is the variation of foot-end force caused by the IC (we call it "impedance force" in the following passage) at sampling time t. Thus, under IC, F^e will take a period of time to converge to F^d by eliminating F_t^{dis}. For example, as shown in the red curve in Fig. 3, in time periods $t_1 \sim t_2$ and $t_3 \sim t_4$, when F_t^{dis} tends to a stable value, the IC can have enough time to eliminate F^{dis} through F^I, so that the F^e gradually tracks F^d.

However, in Fig. 3, when the height of the slope terrain rises fast continuously at the contact points P_n, P_{n+1} and P_{n+2}, the foot-end disturbance force changes rapidly. Under IC, F^e cannot quickly track F^d, as shown by red line in time periods $t_2 \sim t_3$. Therefore, the generation of F^I by IC is always slower than the variable F^{dis}. As a result, F^e can be never stable at F^d when the slope changes rapidly.

Moreover, in order to better describe the reason why IC cannot track the target force under the rapid change of terrain slope, we draw Fig. 4(a). In Fig. 4(a), the red line represents F^e. The blue and green arrow represent F^{dis} and F^I. t_n is the nth sampling time. From Eq. 3, we know that the change of red line equals to the sum of blue arrow and green arrow.

Meanwhile, we assume that IC is effective enough that F_n^e can converge to F^d at the next sampling time t_{n+1}. Due to the zero bias of F_1^e and F^d at time t_1, there will be no F^I in the period between $(t_1, t_2]$. The F^e can only be determined by F^{dis} in this interval, and F^e in the period between $(t_1, t_2]$ can never equal to F^d. With the change of F^{dis} in next period $(t_2, t_3]$, the F^I can only eliminate the bias between F_2^e and F^d at the last sampling time t_2, $F_3^e = F_2^e + F_2^I + F_2^{dis} \neq F^d$. Hence, F^e cannot equal to F^d with an existing F^{dis} in the period between $(t_2, t_3]$. So, under IC, the actual force can't equal to target force with a changing disturb force.

To sum up, when F^{dis} changes rapidly, IC with constant target force cannot make the F^e quickly track F^d, that is, the hysteresis problem. Therefore, we need to design an algorithm that can adaptively change the input target force of the impedance controller according to the change of the disturbance force.

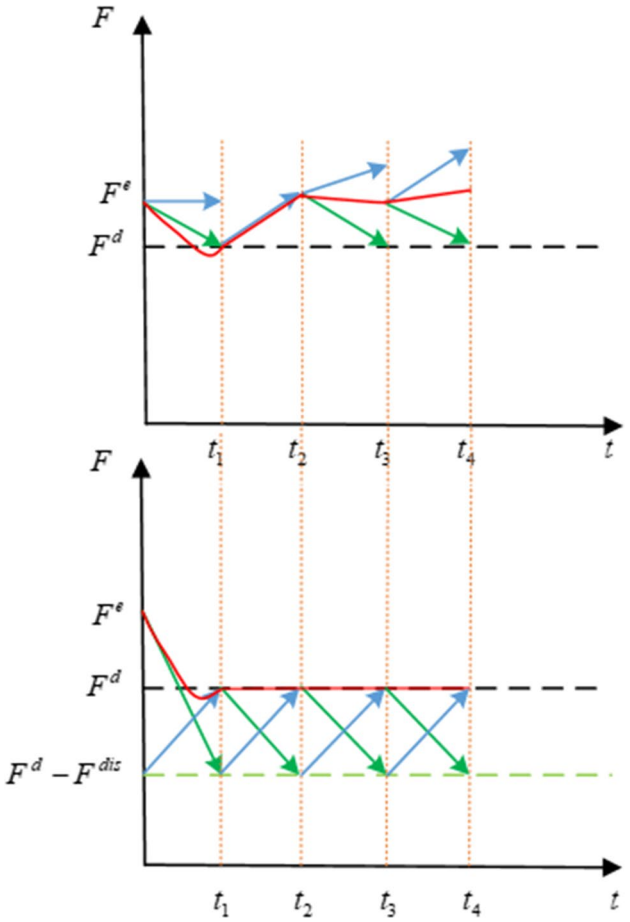

Fig. 4 The variation of foot-end force within little sampling time under the condition of robot driving slope: (**a**) Traditional impedance control principle; (**b**) This paper introduces the principle of variable impedance control

3 Vibration Isolation Control Framework

In Section 2, we established the contact model between the robot's foot-end and the slope terrain, and analyzed the reason why IC could not track the target force when the robot's leg passed through the slope with large angle. In this section, an adaptive impedance control strategy based on variable target force (Fig. 5) is designed to solve the lag problem of IC under constant target force. The strategy is mainly composed of two parts: FDFE and FCAC, which are used to continuously update the input target force F^{di} of the impedance controller, so as to reduce the steady-state force error and enhance convergence speed from F^e to F^d.

In Fig. 6, FDFE including slope angle model, slope terrain model, ARIMA model, and event-triggering mechanism, is used to predict and calculate F^{dis} of terrain on the foot-end that cause the reduction of steady-state force error. FCAC based on a feed-forward control of force, which is used to accelerate the convergence speed of F^e to F^d. Besides, l^c and l^m are the input and output of the electric cylinder position controller after the inverse kinematics and forward kinematics of the single leg respectively. The inverse kinematics and forward kinematics of the single leg have been studied in our previous work [1]. The electric cylinder controller adopts an event triggered auto disturbance rejection control method to realize position tracking and improve the stability of the system [44].

3.1 Theory of FDFE and FCAC

FDFE aims to change the target force of IC to reduce the steady-state error between F^e and F^d. From the following analysis, we find that F^d need to be minused by a bias force

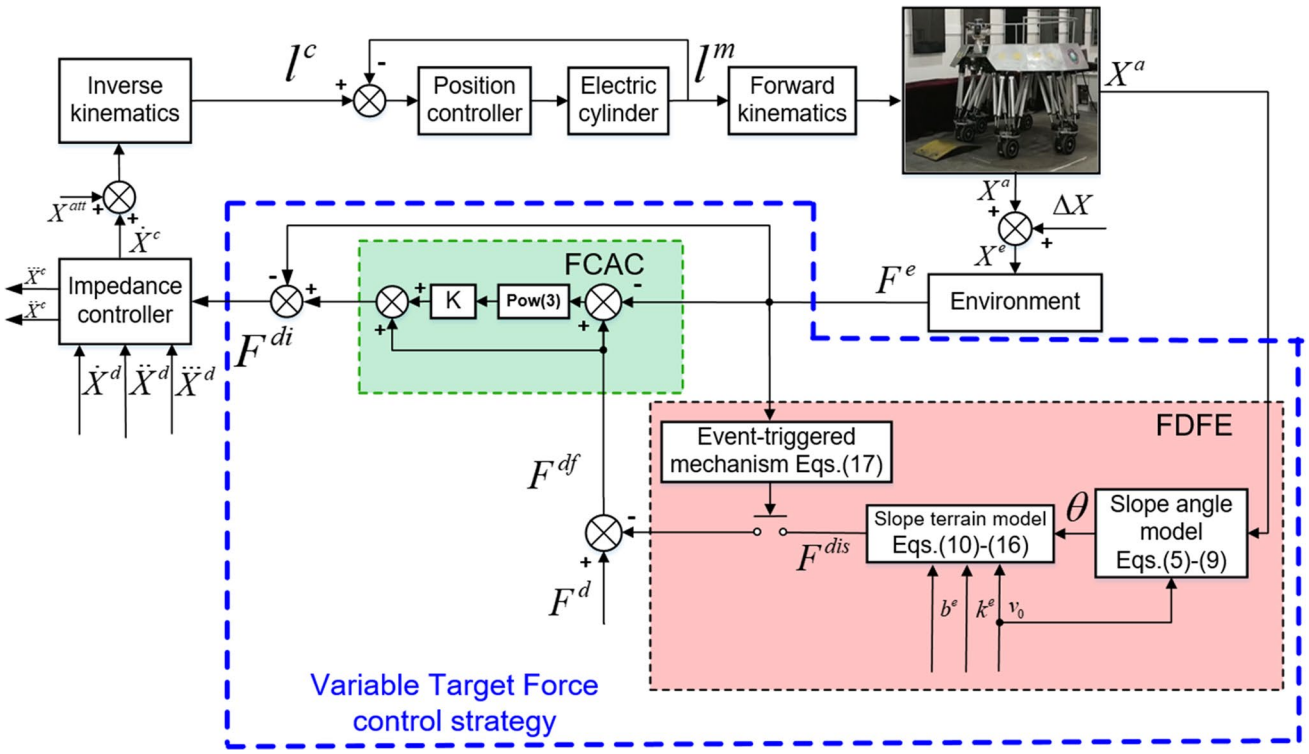

Fig. 5 Adaptive impedance control framework with variable target force for BIT-NAZA-II

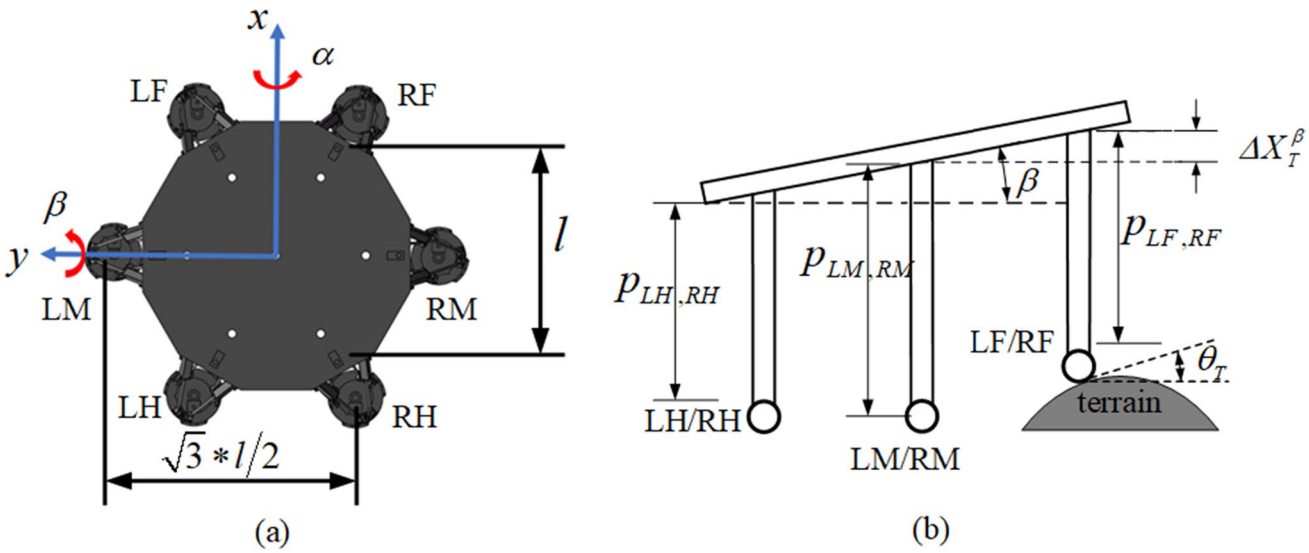

Fig. 6 The slope angle model when the robot passes through the slope terrain

which should be F^{dis} as the foot-end touch the slope. F^{dis} relates to the slope angle, speed of the foot, etc.

We describe the variation of foot-end force within little sampling time in Fig. 4(b). The foot-end force will be $F^e_{t+1} = F^e_t + F^{dis}_t + F^I_t$. The red line represents F^e. The black and green dotted line respectively correspond to the F^d and updated target force F^{df}. The blue and green arrow respectively correspond to the variation of F^{dis} and F^I. We try to keep $F^e_t - F^d = 0$, which means make red line and black dotted line coincide. Impedance force should be

$F_t^I = -F_t^{dis} + F_t^e - F^d$, which means the sum of blue and green arrow in Fig. 4(b) tends to be an arrow parallel to the horizontal axis. So, $F_{t+1}^e = F_t^{dis} + F_t^I + F_t^e = F^d$. There are two points to realize $F_t^I = -F_t^{dis} - F_t^e + F^d$:

1. Enhance the stability and the accuracy of convergence of foot force. The 1st updated force should be $F_t^{df} = F^d + F_t^{dis}$. So, F_t^e can converge to F^d with high accuracy.
2. Accelerate the converge of foot force. There will be an power feed-forward controller between F_t^e and 1st updated force F_t^{df}. It produces the 2nd updated force $F_t^{di} = F_t^{df} + K(F_t^{df} - F_t^e)^m$. With the faster speed of impedance force F_t^I catch up with the minus disturbance force $-F_t^{dis}$, the prerequisite of FDFE can be satisfied.

The FDFE and FCAC respectively realize step 1 and step 2.

3.2 Foot-end Disturbance Force Controller

3.2.1 Slope Angle Model

In Fig. 6, it shows the slope angle model between the robot's foot-end and the terrain when the robot passes through the slope terrain. In Fig. 6, the robot has six legs which are *RF*, *RM*, *RH*, *LF*, *LM*, and *RF* respectively, and the distribution shape of the six legs is a regular hexagon. The length between *RF* leg and *RH* leg is *l*, and the length between *LM* leg and *RH* leg is $\sqrt{3}l/2$. α is the roll angle, β is the pitch angle. In Fig. 6 (b), when the robot passes through the slope terrain at the sampling time *t*, the pitch angle of the body is β_t, and the legs of the robot need to be adjusted by ΔX_t^β in the *Z* direction to maintain the horizontal stability of the attitude. Therefore, at sampling time *t*, the angle θ_t of the terrain slope is expressed as follows

$$\Delta X_t^\beta = Q^\beta (l/2)\sin\beta, \theta_t = Q_t^f \cdot arctan(\frac{\Delta X_t^\beta}{v_0 T}) \tag{4}$$

$$Q_t^f = [{}^{LF}q_t^f, {}^{LM}q_t^f, {}^{LH}q_t^f, {}^{RM}q_t^f, {}^{RM}q_t^f, {}^{RF}q_t^f]^T \tag{5}$$

$${}^{leg}q_t^f = \begin{cases} 1, & {}^{leg}F_t^e > 0 \\ 0, & {}^{leg}F_t^e \le 0 \end{cases} \tag{6}$$

where $Q^\beta = [1, 0, -1, -1, 0, 1]^T$, the leg sequence of matrix ΔX_t is [LF, LM, LH, RH, RM, RF]. Q^f represents the label of whether the leg contact with the ground. Only if the leg touches the ground, we can calculate the slope angle θ_t through theory below. v_0 is the initial travel speed of the robot. β is the pitch angle and is obtained by the attitude sensor. Similarly, when the robot passes through the slope terrain, if the roll angle α_t of the body meets $\alpha_t \neq 0$ at the sampling time *t*, the leg of the robot needs to be adjusted to ΔX_t^α, and meets $\Delta X_t^\alpha = Q^\alpha \cdot \sqrt{3}l/6 \cdot sin\alpha$, where $Q^\alpha = [1, 3, 1, -1, -3, -1]^T$ At the same time, take the length ΔX_t^a and ΔX_t^{att} that have been adjusted by the impedance control and attitude contorller(to control the height and attitude of robot body stable) in to consideration. Therefore, the terrain slope angle θ_t in Eq. 4 can be redefined as follows

$$\theta_t = Q_t^f \cdot arctan(\frac{\Delta X_t^\beta + \Delta X_t^\alpha + \dot{X}_t^a + \Delta X_t^{att}}{v_0 T}) \tag{7}$$

Thus, the ARIMA model is used to predict the slope angle θ in the next sampling time $t+1$, according to the θ before.

$$\theta = \theta_{t+1} = ARIMA(\theta_i | i \in (0, t], i \in integral) \tag{8}$$

3.2.2 Slope Terrain Model

Figure 7 is the dynamic diagram when the foot-end contacts the slope. In order to calculate the disturbing force, we creatively discretize the robot velocity of this problem. We assume that when the sampling interval is small enough, the contact point *P* between the robot's foot and the slope remains unchanged in each sampling interval, until the robot reaches the next sampling time. Thus, a dynamic analysis diagram for a sampling period perpendicular to the slope direction is obtained as Fig. 8. This figure shows the impedance model of vertical contact between the foot-end and the slope. When the terrain slope angle θ, terrain stiffness k_e, damping b_e and the robot speed v_0 are known, the terrain slope model is established to calculate the external disturbance force F^{dis}. The disturbance force F^{dis} in the vertical direction of the foot-end includes the impulse force $F^{incline}$ perpendicular to the slope direction and the speed difference belt force $f^{incline}$ parallel to the slope direction.

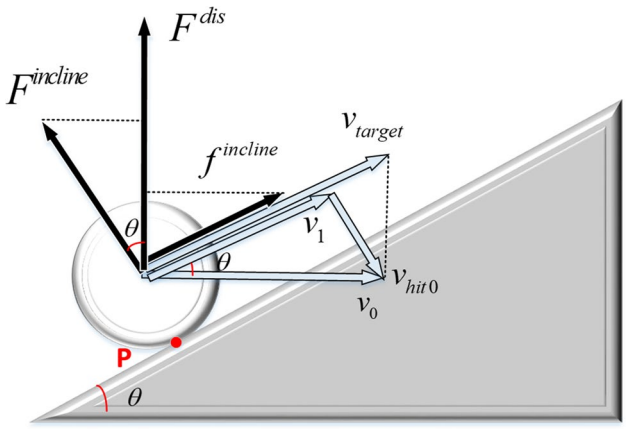

Fig. 7 Schematic diagram of dynamics when the foot-end contacts the slope

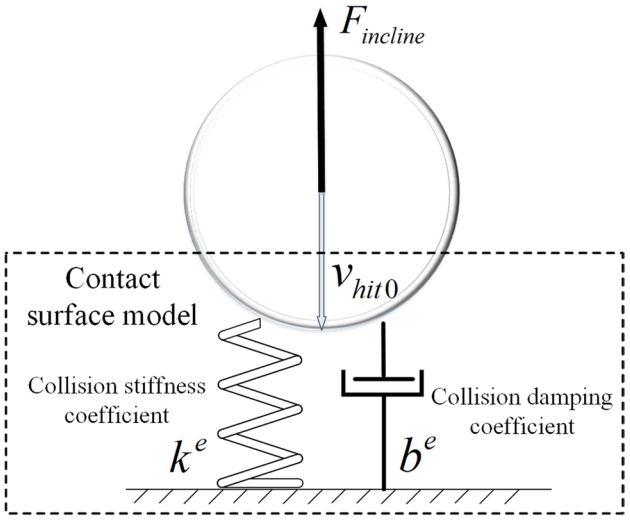

Fig. 8 Impedance model diagram of foot-end and slope in vertical slope direction

In Fig. 7, v_{hit0} represents the speed perpendicular to the slope, which will be offset by the impulse generated by the slope, that is, when the robot's wheel contacts the slope, the foot-end will generate a vertical slope upward force $F^{incline}$ due to the impulse. v_1 represents the actual speed of the foot-end parallel to the slope, and its speed is less than the target speed v_{target} parallel to the slope, so that the foot-end will produce speed difference belt force $f^{incline}$. Therefore, we need to eliminate the foot-end forces $F^{incline}$ and $f^{incline}$ perpendicular to and parallel to the slope, respectively.

(1) *Impulse force* $F^{incline}$: As shown in Fig. 8, when the robot travels with initial speed v_0 until the foot-end contacts the slope, the speed of the foot-end perpendicular to the slope is v_{hit0}, which can be offset by the impulse generated by the slope. Thus, we establish the state space equation between v_{hit0} and $F^{incline}$ as follows

$$\begin{bmatrix} \dot{x_1} \\ \dot{x_2} \end{bmatrix} = \begin{bmatrix} 0 & -1 \\ \frac{k^e}{m^e} & \frac{b^e}{m^e} \end{bmatrix} \begin{bmatrix} x_1 \\ x_2 \end{bmatrix} + \begin{bmatrix} 1 & 0 \\ 0 & -1 \end{bmatrix} u \tag{9}$$

$$y = \begin{bmatrix} k^e & b^e \end{bmatrix} \begin{bmatrix} x_1 \\ x_2 \end{bmatrix} + \begin{bmatrix} 0 & m \end{bmatrix} u \tag{10}$$

where $u = \begin{bmatrix} v_{hit0} = \frac{v_0}{\sin\theta} \\ g\cos\theta \end{bmatrix}$, $y = F^{inline}$. x_1 is the shape variable of the foot-end wheel along the direction perpendicular to the slope. x_2 is the deformation speed of the foot-end wheel in the direction perpendicular to the slope. v_0 is the initial travel speed. θ is the terrain slope angle. m^e is the mass of the single leg. g is the acceleration of gravity. k^e and b^e are the terrain stiffness coefficient and damping coefficient respectively.

When $x(t_0) = 0$, the solution of Eqs. 9 ~ 10 is as follows

$$y(t_x) = \begin{bmatrix} k^e & b^e \end{bmatrix} \int_{t_0}^{t_x} e^{\begin{bmatrix} 0 & -1 \\ \frac{k^e}{m^e} & \frac{b^e}{m^e} \end{bmatrix}(t_x-\tau)} \begin{bmatrix} 1 & 0 \\ 0 & -1 \end{bmatrix} u d\tau + \begin{bmatrix} 0 & m \end{bmatrix} u \tag{11}$$

where t_x is the sampling time, τ is the integral time variable, and t_0 is the contact time between the wheel and the slope. Beside, we can discretize the initial motion speed of the robot. At the beginning of each sampling time t, the impulse force on the foot is equal to the solution of Eq. 11, that is, $F^{inline} = y(\Delta T)$. ΔT is a small period of time.

(2) *Speed difference belt force* $f^{incline}$: In Fig. 7, when the robot travels with initial speed v_0 until the foot-end contacts the slope, the actual speed v_1 and the target speed v_{target} of the foot-end parallel to the slope direction are as follows

$$\begin{cases} v_1 = v_0 \cos\theta \\ v_{target} = \frac{v_0}{\cos\theta} \end{cases} \tag{12}$$

However, considering that the actual speed v_1 is less than the target speed v_{target}, the speed difference between the actual speed and the target speed makes the impedance model of the single leg actuator generate the driving force, and the driving force is described as follows

$$f^{impedance} = B^d(v_{target} - v_1)\sin\theta + K^d X^a \tag{13}$$

where B^d and K^d represent the target stiffness and target damping of the single leg impedance model respectively. X_t^a is the actual position of foot-end in the Z-direction at the sampling time t. Thus, the calculation formula of speed difference belt force $f^{incline}$ is described as follows

$$f^{incline} = \frac{f^{impedance}}{\sin\theta} \tag{14}$$

According to Eqs. 9 ~ 14, the F^{dis} can be described as follows

$$F^{dis} = F^{incline}\cos\theta + f^{incline}\sin\theta \tag{15}$$

3.2.3 Event-triggered Mechanism

We hope the calculated slope angle θ by above method be similar to the real slope angle θ^{real}, to enhance the accuracy of dynamic algorithm results.

However, when the robot walks on the actual road, the foot end force may be disturbed by small stones, wind

pressure and other environmental aspects. It makes the algorithm of predicting the slope angle through the actual foot end force cause errors, and then leads to great error of calculated disturbing force F^{dis} and the reduction of force control stability. Therefore, we design an event-triggered mechanism to eliminate F^{dis} which may be greatly affected by the environmental aspects except slope. When the actual force F^e or the final target force F^{df} exceeds the maximum force threshold, the foot tip can be defined as contacting a slope with a certain slope. Furthermore, the ramp F^{dis} is removed in the target force F^d, otherwise the F^{dis} is not removed.

$$\Gamma(t) = \begin{cases} 1, & \text{if } \forall\ \tau \in (t, t+\Delta T), \exists\ |F_\tau^e - F^d| \geq \Delta F_{max} \\ & \text{or } |F_\tau^{df} - F^d| \geq \Delta F_{max} \\ 0, & \text{otherwise} \end{cases} \tag{16}$$

where F^d is target force. F^e is foot-end contact force. ΔF_{max} is the maximum deviation between the actual contact force and the target force.

3.2.4 Implement of Impedance Control with FDFE

To facilitate the implementation in the actual robot controller, impedance control with FDFE can be converted into the following discrete forms

$$\begin{cases} \ddot{X}_{t+1}^a = \ddot{X}_t^a - \frac{1}{M^d}[(F_t^e - F^{di}) - B^d(\dot{X}_t^a - \dot{X}_{t+1}^d) \\ \qquad - K^d(X_t^a - X_{t+1}^d)] \\ \dot{X}_{t+1}^a = \ddot{X}_{t+1}^a \times T + \dot{X}_t^a \\ \dot{X}_{t+1}^a = \ddot{X}_{t+1}^a \times T + \dot{X}_t^a \\ \theta_t = Q_t^f arctan(\frac{\Delta X_t^\alpha + \Delta X_t^\beta + \dot{X}_t^a + \Delta X_t^{att}}{v_0 T}) \\ \theta_{t+1} = ARIMA(\theta_\tau | \tau \in [0,t], \tau \in integral) \\ F_{t+1}^{incline} = y(T), u = \begin{bmatrix} \frac{v_0}{\sin\theta_{t+1}} \\ g\cos\theta_{t+1} \end{bmatrix} \\ F_{t+1}^{dis} = F_{t+1}^{incline}\cos\theta_{t+1} + B^d(\frac{v_0}{\cos\theta_{t+1}} - v_0\cos\theta_{t+1})\sin\theta_{t+1} + K^d\dot{X}_{t+1}^a \\ F_{t+1}^{df} = F^d - F_{t+1}^{dis}\Gamma(t+1) \end{cases} \tag{17}$$

where T is the system communication cycle between the host controller and the sub controller. The control schematic of VTFIC is shown in Fig. 9.

3.3 FCAC

In Fig. 5, FCAC is designed based on power functional feed-forward controller of F^e and 1st updated target force F^{df}. Feed-forward controller can be used to accelerate the convergence of Impedance force F_t^I to disturb force F_t^{dis}. Form Fig. 5 we know it can assist the convergence of F^e to F^{df}. To implement the FCAC, as shown in Fig. 9. we convert it into following discrete forms

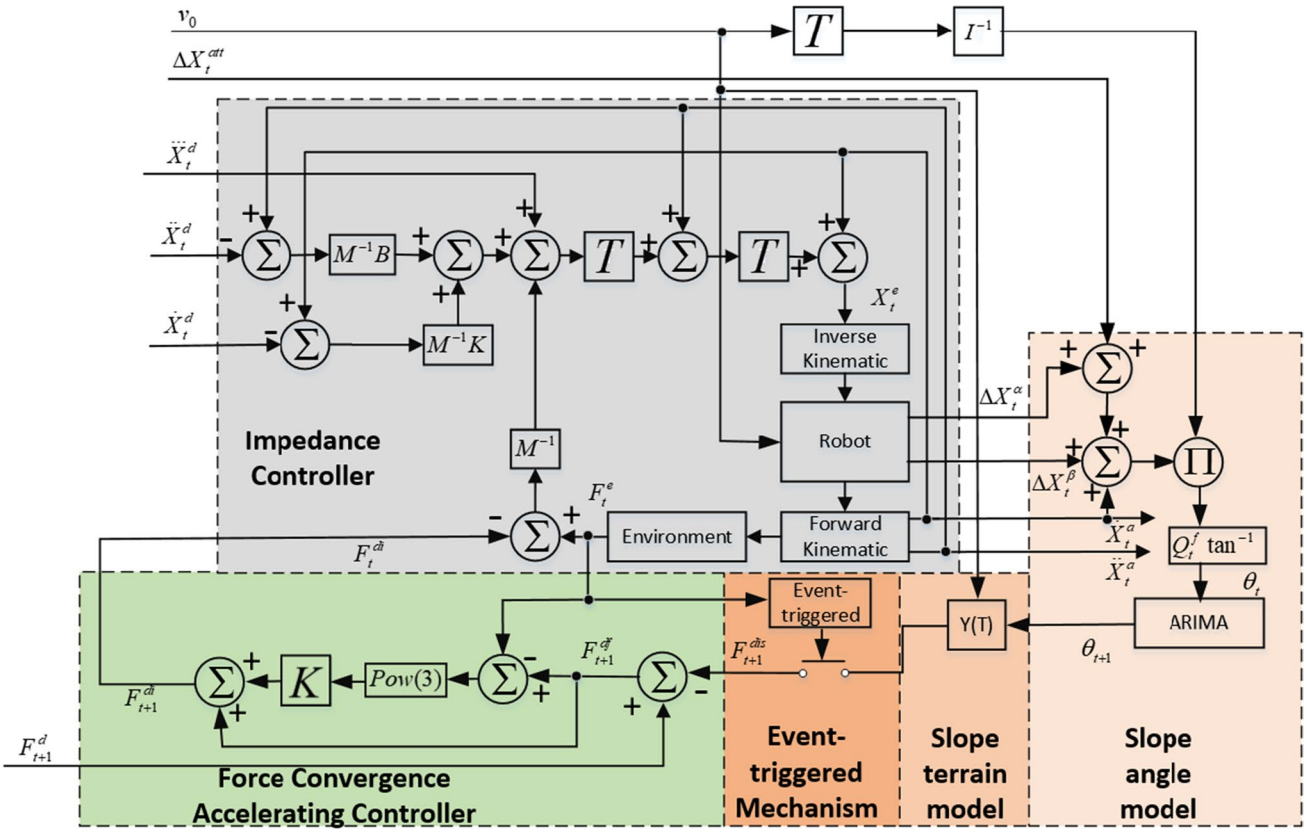

Fig. 9 The control schematic of variable target force impedance control

$$F_t^{di} = F_t^{df} + Feed(x) = F_t^{df} + K \cdot (F_t^{df} - F_t^e)^m \cdot (SIGN(F_t^{df} - F_t^e))^{m+1} \tag{18}$$

where m represents the power of error correction speed. $SIGN$ is signum function. In order to show the effect of FAFC system on accelerating the tracking speed of target force, we built control simulation environments under different feed-forward controller in FAFC with same value of impedance parameters. We try to make the actual force follow the target force $F^{df} = 600N$ from 0.

As shown in Fig. 10, the feed-forward control of linear function (first-order power function, $Feed(x) = K(F_t^{df} - F_t^e)$), logarithmic function ($Feed(x) = ln(F_t^{df} - F_t^e)$), second-order power function ($Feed(x) = K \cdot (F_t^{df} - F_t^e)^2 \cdot (SIGN(F_t^{df} - F_t^e))^3$) and no function is simulated (K value in linear function and second-order power function are the same). We assume that it is basically stable around 10% of the target value, and find that the stability time of the above feed-forward control function is 2.3s, 5s, 5.4s and 6.3s respectively. Among them, the convergence speed of power function is the fastest. Furthermore, as shown in Fig. 11, we simulated the power function feed-forward control effect of different orders (0, 2, 3, 4). The value of K from each orders(m) can make the output stable at its fastest speed without output vibration or divergence, which can also sustain the disturbance of 5000N. It is found that the basic stability time of the controlled object is 6.3s, 2.3s, 1.3s and 3.4s respectively with the increase of the power function order. Since there is no overshoot in the feed-forward of the third-order power function and its convergence speed is much faster comparing with the convergence speed with other feed-forward controller, we choose the third-order power ($m = 3$) function as the feed-forward controller.

In view of the possible vibration caused by power function feed-forward, we limit the linear velocity of the robot's foot end in the Z direction to reduce the impact of the foot end on the ground and thus slow down the vibration. ($\dot{X}^c = 1m/s, if \dot{X}^c > 1m/s.$) Through the event triggering mechanism, we eliminate the high frequency small amplitude disturbance force F^{dis} output by FDFE, reduce the possibility of high frequency oscillation of FCFA input force F^{df}, and reduce the problem of low stability of the system. In addition, according to the proof of stability, power function type feed-forward control is theoretically stable. We try the proper value of K so that the system can follow the target force F^{di} with disturbance up to 5000N and enhance the stability of the system in the face of disturbances.

In a word, the power function feed-forward control can quickly calculate the disturbance and directly adjust the input significantly and roughly, which can greatly improve the slow convergence speed of large inertial (mass) objects under feedback force control and the possible existence of steady-state errors.

3.3.1 Proof of Stability

In this section, the global asymptotic stability of the FCAC system is proved, and the value range of the power function feed-forward coefficient K is calculated.

Substituting Eqs. 18 into 1, according to the experiment $\ddot{X}^d = 0, \dot{X}^d = 0, \dot{X}^d = 0$, we have:

$$M^d \ddot{X}_t^a + B^d \dot{X}_t^a + K^d \dot{X}_t^a = K \cdot (F_t^e - F^{df})^3 + F_t^e - F^{df} \tag{19}$$

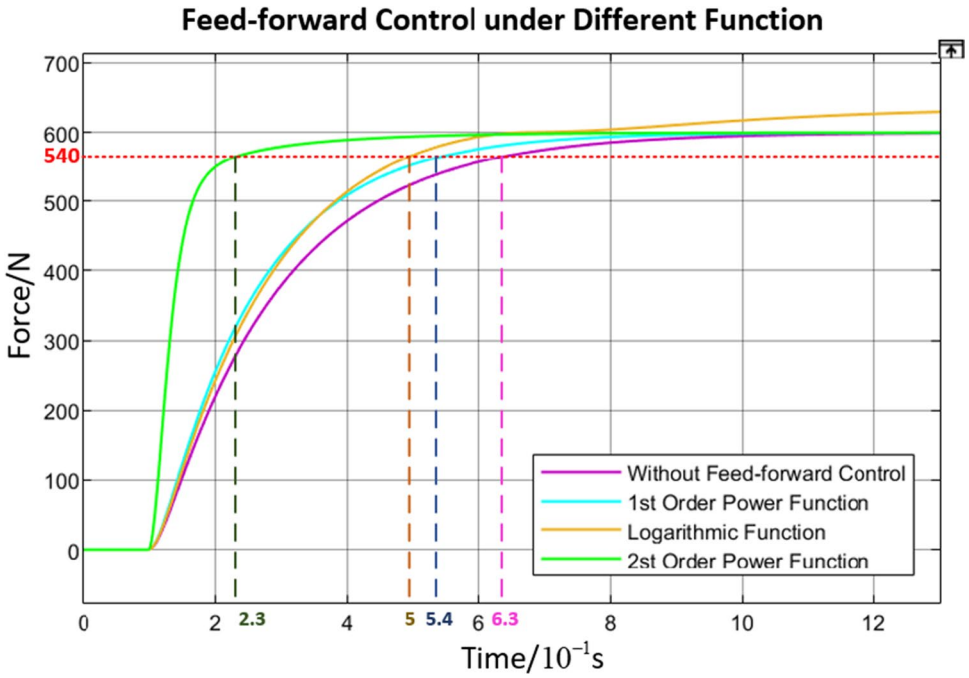

Fig. 10 Tracking process with different or without feed-forward control

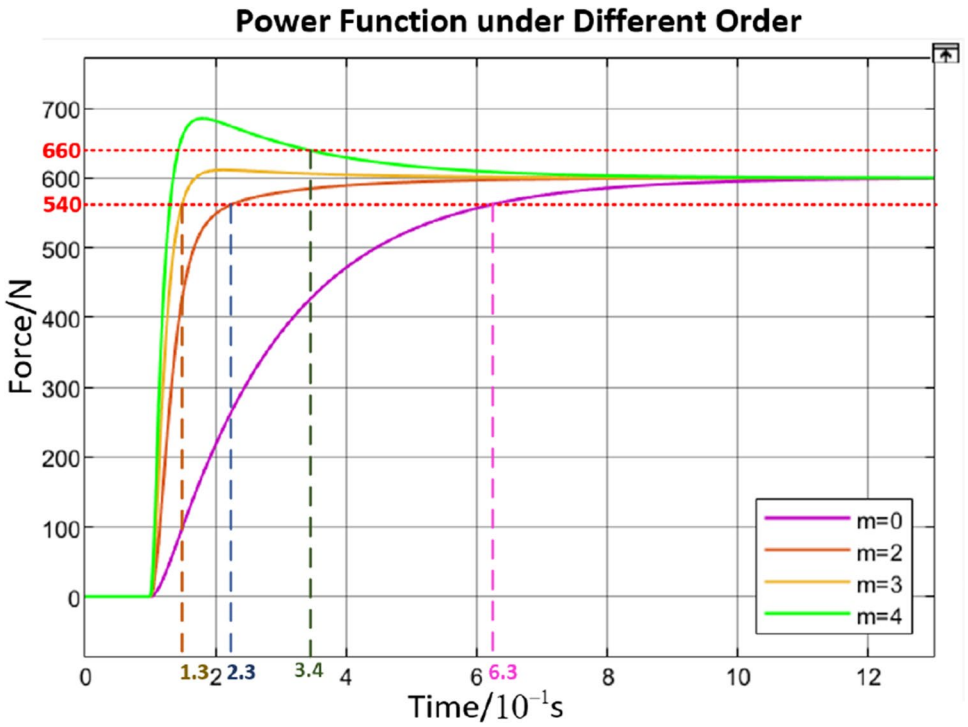

Fig. 11 Tracking process under feed-forward control with different order

We try to prove the stability of the system when the foot tip and the ground is always in contact. Therefore, $X_t^e = X_t^a$ the relationship between F_t^e and X_t^e can be inferred from Eq. 2:

$$\dot{F}_t^e = -m^e \dddot{X}_t^a - b^e \ddot{X}_t^a - k^e \dot{X}_t^a \tag{20}$$

Therefore, we can construct the control block diagram of the system as Fig. 12.

where $F_t^x = F_t^e - F^{df}$. We see $x_1 = \dot{X}_t^a, x_2 = \ddot{X}_t^a, x_3 = F_t^x$. So the state space of the system is as follows:

$$\begin{bmatrix} \dot{x}_1 \\ \dot{x}_2 \\ \dot{x}_3 \end{bmatrix} = \begin{bmatrix} x_2 \\ \frac{1}{M^d}(-K^d x_1 - B^d x_2 + K(x_3)^3 + x_3) \\ (\frac{m^e K^d}{M^d} - k^e)x_1 + (\frac{m^e B^d}{M^d} - b^e)x_2 - \frac{m^e K}{M^d}(x_3)^3 - \frac{m^e}{M^d}x_3 \end{bmatrix} \tag{21}$$

We use Lyapunov's second method to prove the stability of the above nonlinear system. First, we construct a positive definite energy function $V(x) = (b^e x_1 + m^e x_2 + x_3)^2 \geq 0$. We derive the energy function $V(x)$ as follows:

$$\begin{aligned} \dot{V}(x) =& 2(b^e x_1 + m^e x_2 + x_3)(b^e \dot{x}_1 + m^e \dot{x}_2 + \dot{x}_3) \\ =& -2b^e k^e (x_1)^2 - 2m^e k^e x_1 x_2 - 2k^e x_1 x_3 \\ =& x^T \begin{bmatrix} -2b^e k^e & -m^e k^e & -k^e \\ -m^e k^e & 0 & 0 \\ -k^e & 0 & 0 \end{bmatrix} x \end{aligned} \tag{22}$$

The order principal sub formulas of the above matrices are $\pi_1 = -2b^e k^e < 0, \pi_2 = 0, \pi_3 = 0$. So the derivative of the energy function $\dot{V}(x)$ is semi negative definite. Because $\dot{V}(x)$ is not always 0 except the origin. And, when $||x|| \to \infty, V(x) \to \infty$. So the system is globally asymptotically stable.

4 Simulation and Experiment Validation

In order to verify the effectiveness of the variable target force impedance method proposed in this paper and compare it with IC, simulation (PyCharm and CoppeliaSim) and

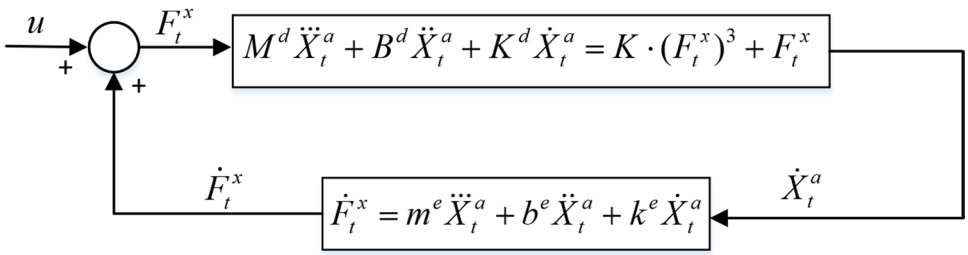

Fig. 12 Control block diagram of the system

experiment are carried out in this section. Thus, the two scene comparison simulation and experiment are performed as follows

1. Co-simulation and experiment of vibration isolation control strategy with different driving speed, such as single slope terrain and multi-slope terrain, is designed to verify the rapidity and stability of the foot-end force tracking target force.
2. In contrast, in order to further verify the superiority of VTFIC algorithm, the comparative simulation and experiment of IC and VTFIC are carried out in single slope and multi-slope terrain.

4.1 Simulation Results of Vibration Isolation Control Under the Single Slope Terrain

Figures 13 and 15 show the simulation scene of vibration isolation control of wheel-legged robot. The forward direction of the robot is along the X-axis, the height, length and width of the slope are $0.1m$, $0.725m$ and $0.3m$ respectively. The robot has six legs, namely LF, LM, LH, RH, RM and RF. The simulation experiment parameters are set as follows: the impedance controller parameters in the Z-direction are $M^d = 2kg \cdot s$, $B^d = 500N \cdot s^2/m$, $K^d = 8N \cdot s/m$. The second-order model parameters of slope terrain are $m^e = 66.7kg$, $b^e = 4000N \cdot s/m$ and $k^e = 5000N/m$ respectively. When the robot is stationary on the flat ground, the target force of RM F^d is $600N$. The ΔF_{max} in event-trigger system equals to $150N$. In the simulink, we tried the K value of different orders of magnitude. When $K = 0.000045$, the system can still maintain fast convergence under the disturbance of 5000N, and will not vibrate or diverge.

The simulation in Fig. 13 is used to prove the necessity of the event triggering mechanism (16). The simulation compares the operation state of the robot in the process of crossing the muddy road with or without the event triggering mechanism under the VTFIC algorithm in speed of 1m/s. Figure 14 shows the actual force and variable target force under the comparative simulation. It is found that without the event triggering mechanism, the change range of the variable target force is large to ±500N, resulting in the instability of the foot force. After taking use of event triggering mechanism, the elimination of small disturbance force F^{dis} reduces the low accuracy of high-frequency disturbance force F^{dis} estimation of foot end caused by small stones on the ground, which further reduces the vibration of foot end force (Fig. 15).

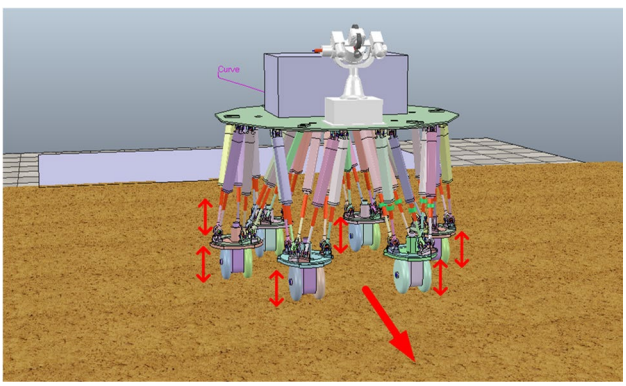

Fig. 13 Simulation scene of robot on muddy road

Under the VTFIC methods, the process of wheeled crossing slope is shown in Fig. 16. In the simulation experiment, the robot is driven by wheels at a constant speed of $0.5m/s$, $1m/s$, $1.5m/s$ and $2m/s$ respectively. Under the comparison of VTFIC and IC algorithm control, the simulation results of RM position on the $X-Z$ plane, foot-end force and body attitude angle are shown in Fig. 17~19.

As shown in Fig. 17, the experimental data record the actual slope position and foot-end of RM trajectory when the robot crosses the slope terrain at different speeds by using VTFIC and IC algorithms. As can be seen from Figs. 16 and 17, We can find that the foot-end position of the robot's RM always coincides with the ground at $0 \sim 0.57m$, and the robot's RM starts to contact the slope at $0.57m$ and drives over the slope at $1.42m$. In Fig. 17, under the control of IC algorithm, the foot-end position of RM cannot coincide with the slope position during driving the slope terrain. Moreover, when the travel speed of the robot is increased, the foot-end position tracking error will be much larger under the control of IC algorithm, especially in the downslope process of the robot. In contrast, under the control of VTFIC, the foot-end position of robot's RM always coincides with the actual position of slope terrain. Even if the robot travels at the speed of $2m/s$, the foot-end position can better fit the actual slope. Therefore, compared with IC algorithm, VTFIC algorithm can greatly reduce the position tracking error of robot in the process of high-speed motion.

Figure 18 shows the foot-end contact force of RM when the robot passes through the slope terrain at the typical speed of $1m/s$ and $2m/s$ respectively under the control algorithms VTFIC and IC. We found that with the increase of the speed of the robot passing through the slope terrain, the foot-end force of RM deviates from the target force more under the control of IC algorithm. The foot-end force deviation is particularly obvious in the downslope process, that is, the foot-end force of RM is maintained below $0N$ for a long time, indicating that RM is suspended. In addition, we can also see from Fig. 18a and b that when the driving speed of the robot reach $2m/s$, even if the robot's RM has passed the slope, the IC control algorithm cannot make the foot-end force track the target force, which illustrates the lag problem of the IC control algorithm. In contrast, under the two speeds of the

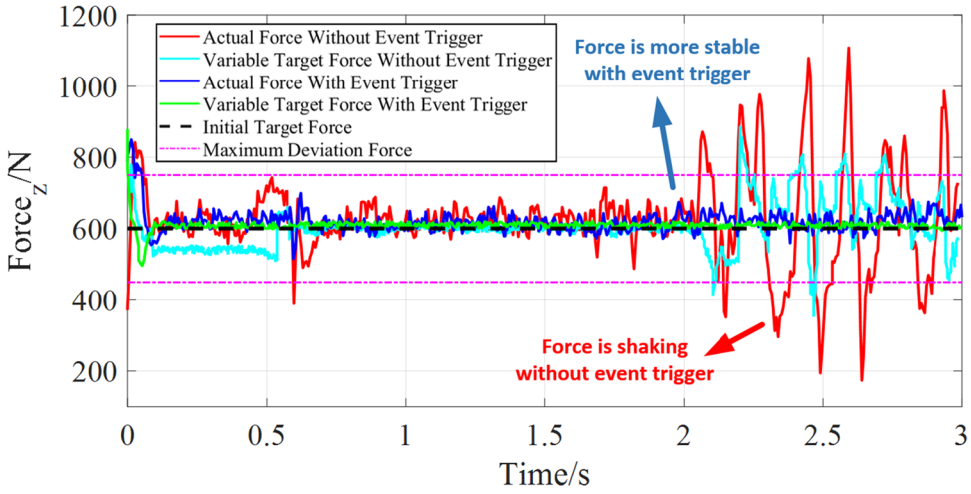

Fig. 14 Foot-end force of RM when the robot crosses muddy road with or without event-trigger under VTFIC

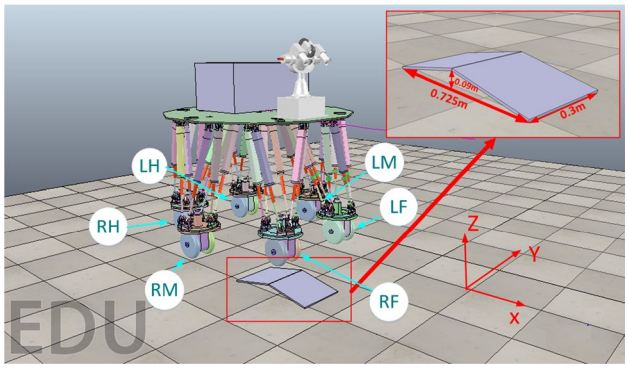

Fig. 15 Simulation scene of robot in a single slope terrain

robot, VTFIC can make the foot-end contact force of RM more stable near the target force. Even if the driving speed of the robot is $2m/s$, the foot-end force of the robot's RM can still better track the target force. When both the actual force F^e and the variable target force F^{df} are within the maximum deviation force ΔF_{max} range, the event trigger mechanism is activated (outputs 0) to reduce the possible force oscillation problem. By observing the data, it can be found that when the foot end of the robot is on a flat ground or the actual force F^e and the variable target force F^{dis} are both within the maximum deviation force range ΔF_{max}, the event trigger mechanism outputs 0, which prevents the FDFE from working, thereby reducing the occurrence of vibration. The change direction of the variable target force is always opposite to the change direction of the actual force to enhance the convergence speed of the actual force.

In order to better evaluate the convergence rate of the foot-end force to the target force, we define the deviation degree of the force as:

$$dev_f = \sqrt{\sum_{i=0}^{n}(F_i^e - F^d)^2/n} \tag{23}$$

where n is the total sampling time. The smaller the force deviation, the higher the force tracking accuracy. Under different driving speeds, the deviation degree between the foot-end force and the target force controlled by VTFIC and IC algorithms is shown in Table 2. We can see that larger the speed of robot, the larger the force deviation degree of

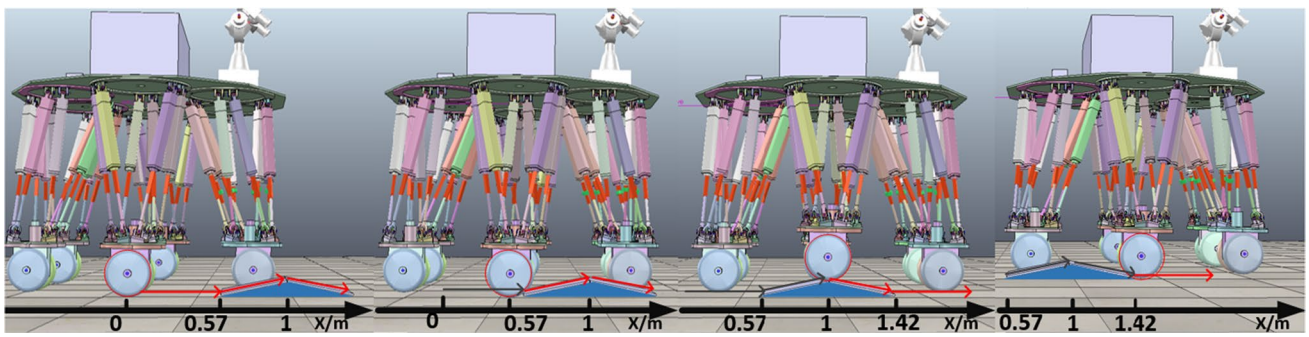

Fig. 16 Scene of snapshots of robot driving over the slope-like terrain by using VTFIC

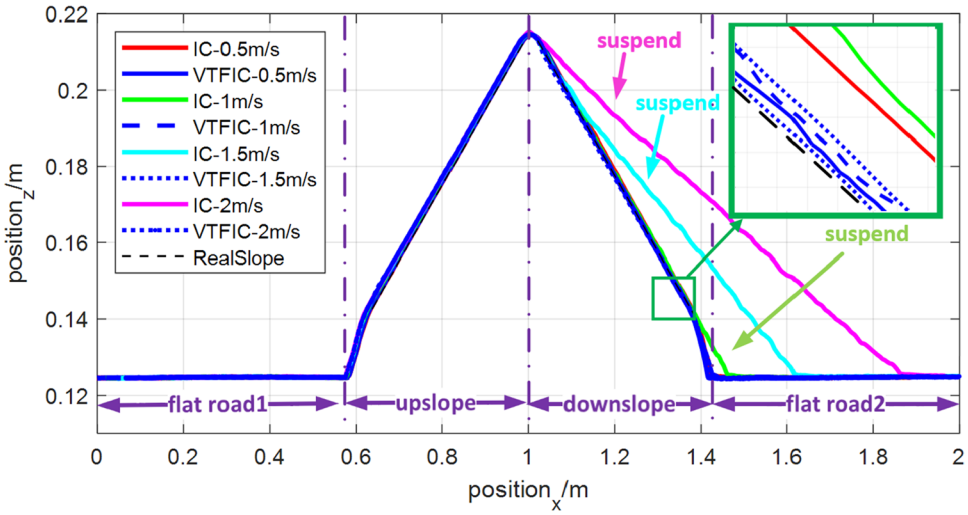

Fig. 17 Foot-end Position tracking of RM when the robot crosses the slope terrain at different speeds by using VTFIC and IC algorithms

each phase (including flat road1, upslope, downslope, flat road2). The deviation degree under VTFIC reduces to less than 80% of it under IC in every phase and speed. Especially, the force deviation degree can be greatly weaken to 18.8% in the downslope phase and 1m/s speed by the VTFIC comparing with IC.

Figure 19 exhibits the attitude of body when the RM crosses the single slope terrain at different speeds by using VTFIC and IC algorithms. We found that the attitude angle (pitch and roll angle) of the robot body reached more than ±5.0° during the process of driving at different speeds under the control of IC algorithm, which proves the poor stability of IC algorithm. In contrast, due to the superior force tracking performance of VTFIC algorithm, the attitude angle of the body is kept within ±1.82° at different motion speeds, and the posture of the body quickly converges to the target attitude angle when the robot changes from slope terrain to flat terrain.

Similarly, we define the attitude deviation degree to evaluate the convergence rate between the actual attitude angle and the target attitude angle. The attitude deviation is described as follows:

$$dev_{\alpha} = \sqrt{\sum_{i=0}^{n} (\alpha_i^e - \alpha^d)^2 / n} \tag{24}$$

where n is the sampling time. The angle deviation is shown in Table 3. Under the control of IC algorithm, dev_a reaches above 1.7°, and the maximum value is 3.4°. In contrast, under the control of VTFIC algorithm, the angle deviation is kept below 0.7°. The greatest undermine of dev_a can be 79.4% with the VTFIC replacing IC. In a word, the actual attitude of robot body will be more stable to target attitude under the controller of VTFIC compared with IC.

4.2 Experiment Results of Vibration Isolation Control Under the Multi-slope Terrain

The experiment in this subsection is carried out under the environment of multiple slope obstacles, Fig. 20. During the walking process of the robot, leg RH, RM, RF and RM have to pass through 1 deceleration zones respectively. Speed bumps have two size, and its height, width and length are 12cm (or 7cm), 42cm and 82cm. The target force is $F^d = 650N$. The other parameter settings of the experiment are the same as those of the previous subsection. We compare the running state of the robot in the process of wheel motion at the speed of 1m/s under the two algorithms. We continue to collect and analyze the experimental data.

We select the position data of the typical foot end RM, RF and LM for drawing and analysis, as shown in Fig. 21. RM (RF, LM) contacts the first uphill at 0.4m (1.56m, 2.38m), reaches the top of the slope at 0.84m (2m, 2.82m), returns to the flat at 1.28m (2.44m, 3.26m) in X axis. During these process, the position tracking accuracy of each leg will be affected by the position tracking error of other legs. It is found that the maximum position error of foot end in Z direction will increase to 0.02m under IC, while the maximum error is only 0.0038m under VTFIC. It can be seen that in complex terrain, the error of VTFIC for position tracking will be greatly reduced to 19% compared with the original IC algorithm.

We draw the Z-direction foot end force trajectory of six legs at the speed of 1m/s, as shown in Fig. 22. Under the IC algorithm, the force tracking error of each leg will reach more than 1000N, and there will be plenty of suspension time of more than 0.2s, which will greatly affect the stability of the fuselage, while the force tracking error of

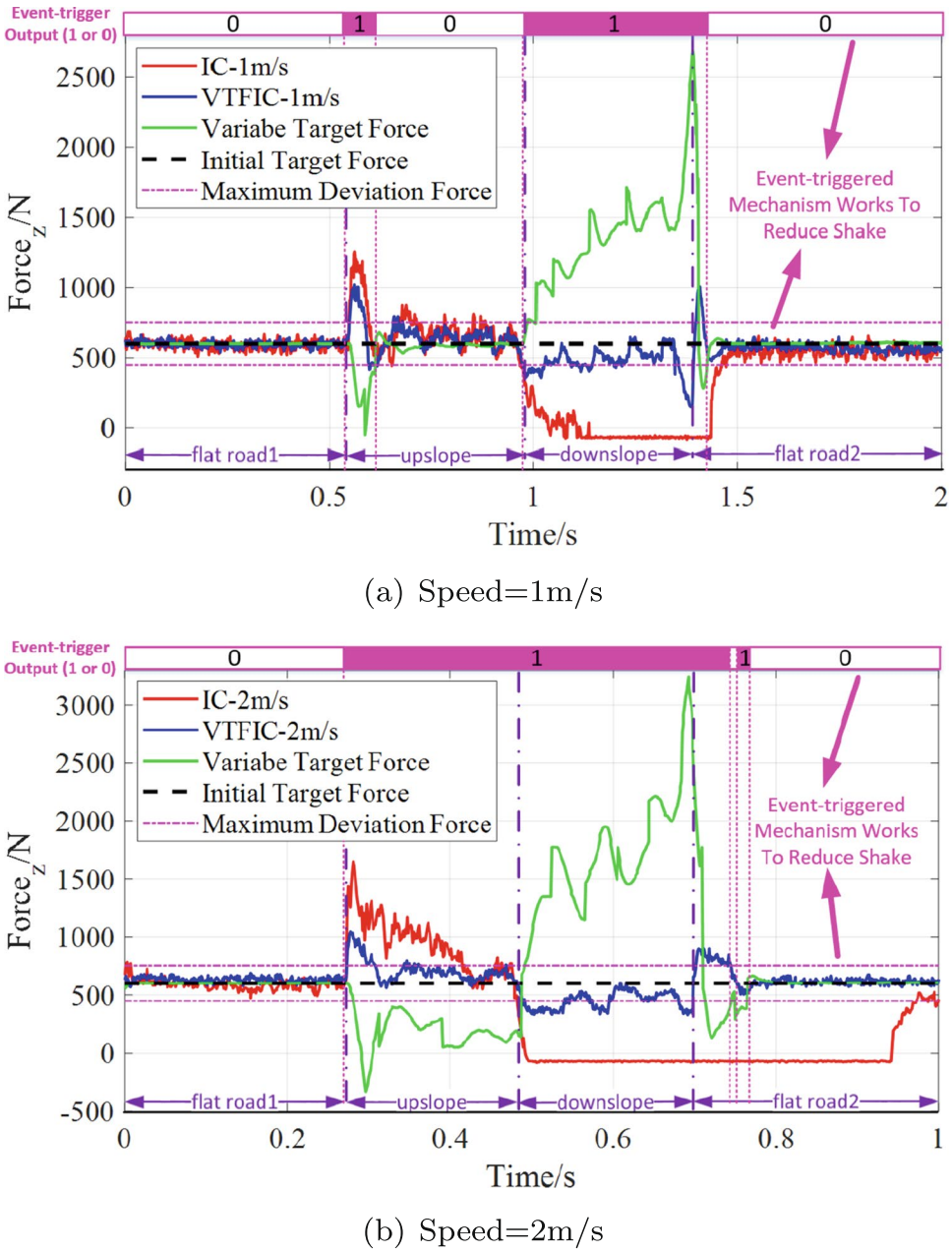

Fig. 18 Foot-end contact force of RM when the robot crosses the slope terrain at different speeds by using VTFIC and IC algorithms

VTFIC in the multi-deceleration belt environment is within 650±200N. When the actual force F^e or variable target force F^{di} at the foot end of the robot deviates greatly, the event trigger mechanism outputs 1. It controls the FDFE to work, and the estimated disturbing force F^{dis} is removed from the target force F^d to accelerate the convergence of the actual force F^e to the target force F^d. As shown in Table 4, the average deviation force (23) of six legs will reduce to 36.8% by the proposed improved algorithm (VTFIC) with little vibration, which will greatly improve the stability of the fuselage during movement.

In Fig. 23, we draw some typical attitude angle curves of the fuselage. It is found that the maximum attitude angle error of the fuselage under IC will reach 7.67°, while the attitude angle error under VTFIC is always within 2.2°. After the IC algorithm is improved, the peak value of angle error is reduced to less than 28.7%. Based on these attitude angle data, we calculate the attitude deviation degree to measure the degree of offset value. As shown in Table 4, Under IC, fuselage roll and pitch offset deviation is 1.65° and above, while under VTFIC angle will be reduced to less than 0.92°. The maximum attitude angle deviation of the fuselage under

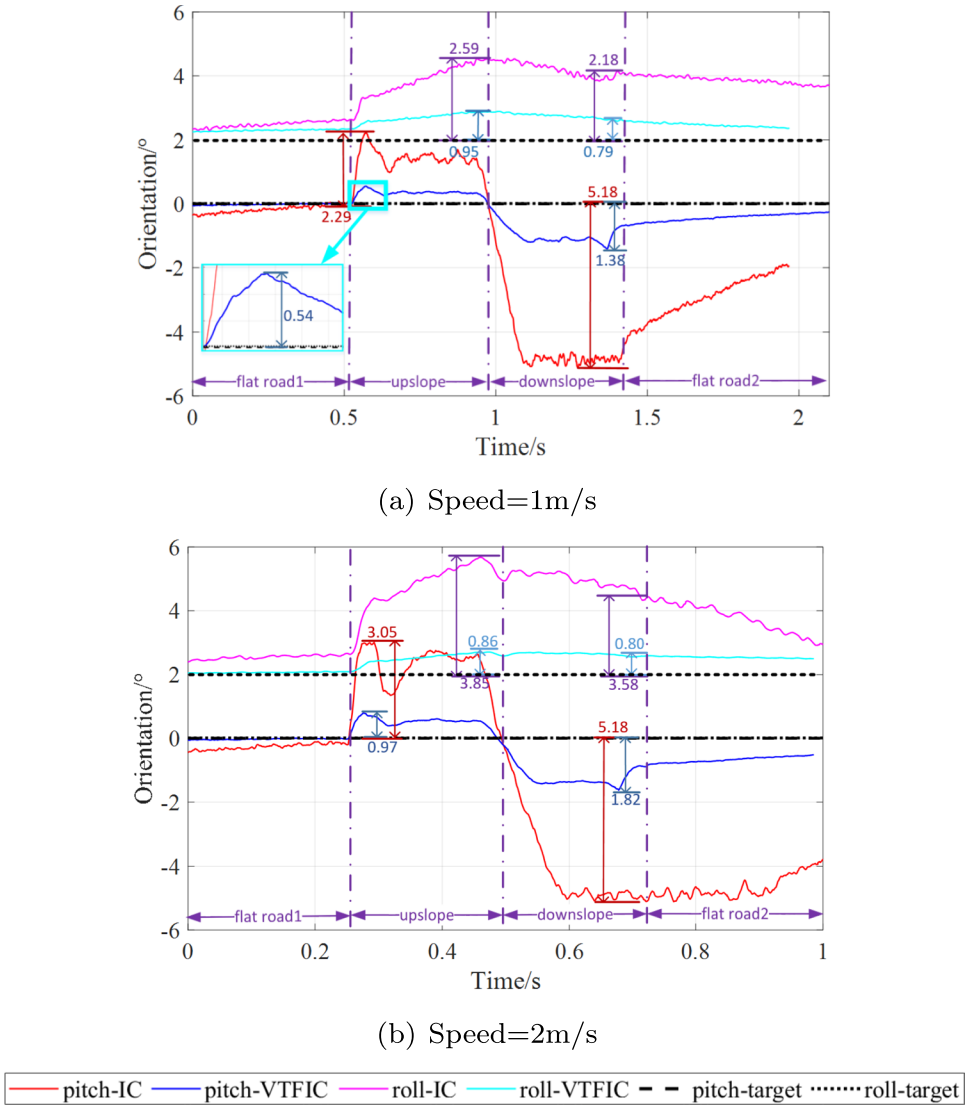

(a) Speed=1m/s

(b) Speed=2m/s

(c) Label definitions for curves

Fig. 19 Attitude of robot's body when the RM crosses the single slope terrain at different speeds by using VTFIC and IC algorithms

Table 2 Foot-end contact force deviation degree of RM when the robot crosses the slope terrain at different speeds by using VTFIC and IC algorithms

dev_f/N	flat road1	upslope	downslope	flat road2
1m/s-IC	34.7	166.3	553.1	181.3
1m/s-VTFIC	25.6	71.2	104.2	66.3
2m/s-IC	43.1	375.1	673.1	512.7
2m/s-VTFIC	25.8	91.7	151.9	108.7

Table 3 Attitude deviation degree of body when the robot crosses the single slope terrain at different speeds by using VTFIC and IC algorithms

$dev_a/°$	1m/s	2m/s
IC-roll	1.7	2.1
VTFIC-roll	0.6	0.5
IC-pitch	2.7	3.4
VTFIC-pitch	0.5	0.7

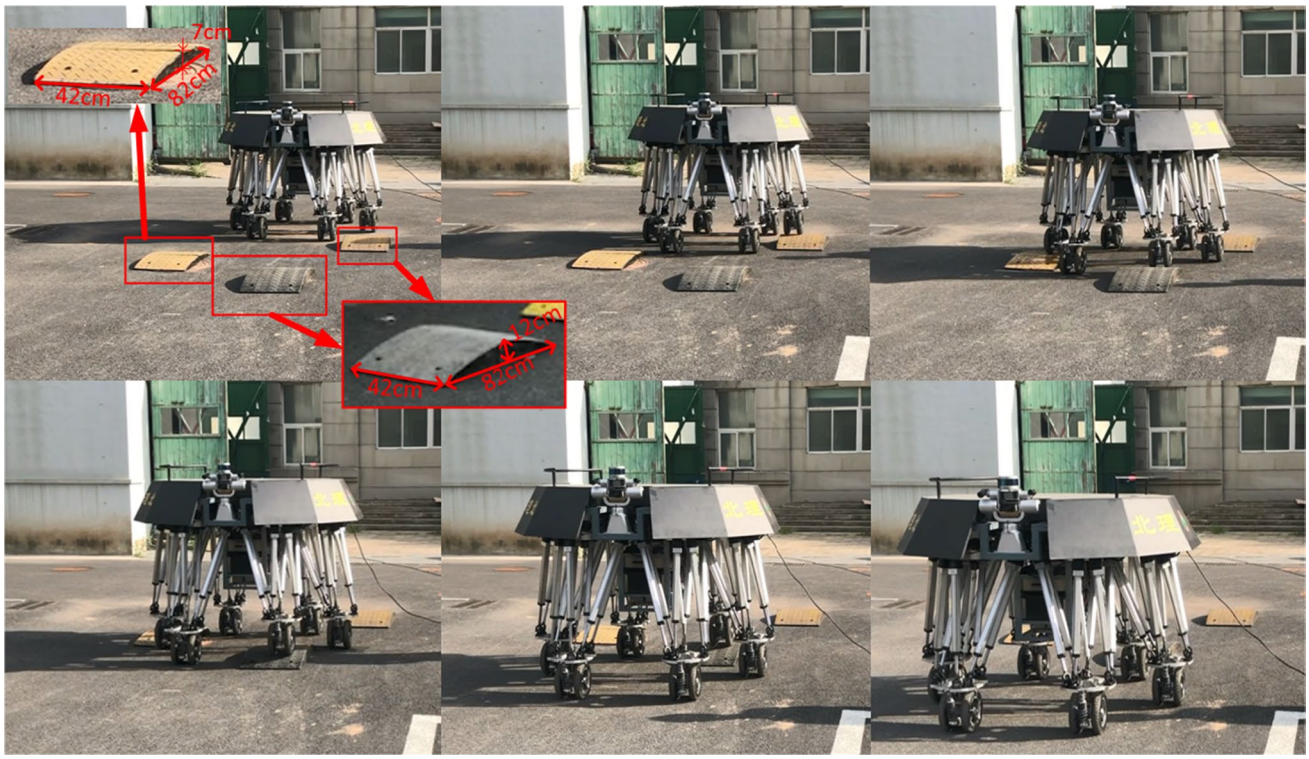

Fig. 20 Experiment with multiple Deceleration zone

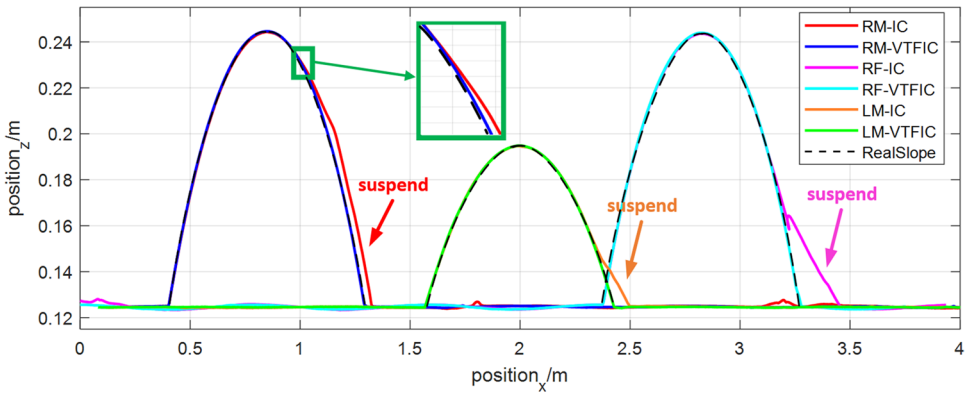

Fig. 21 Position tracking of RM, RF and LM foot-end from multiple slope experiment

VTFIC is reduced to 27.3% compared with IC. The use of VTFIC algorithm will greatly improve the stability of the fuselage, especially under the high-speed movement of the robot.

In order to evaluate the effect of VTFIC in more challenging environment, we conducted experiments in actual rugged outdoor environment. As shown in the Fig. 24, under the VTFIC, the robot can move in wheel mode with high stability on outdoor rough roads.

5 Conclusion

To better solve the problem of foot-end contact force convergence, the VTFIC strategy is proposed, which increases the foot-end force tracking speed and accuracy by adaptively changing the target force of impedance control, so that the robot has better stability in the process of dynamic motion on rough ground. The theoretical basis and calculation process of the adaptive change rule of target force are

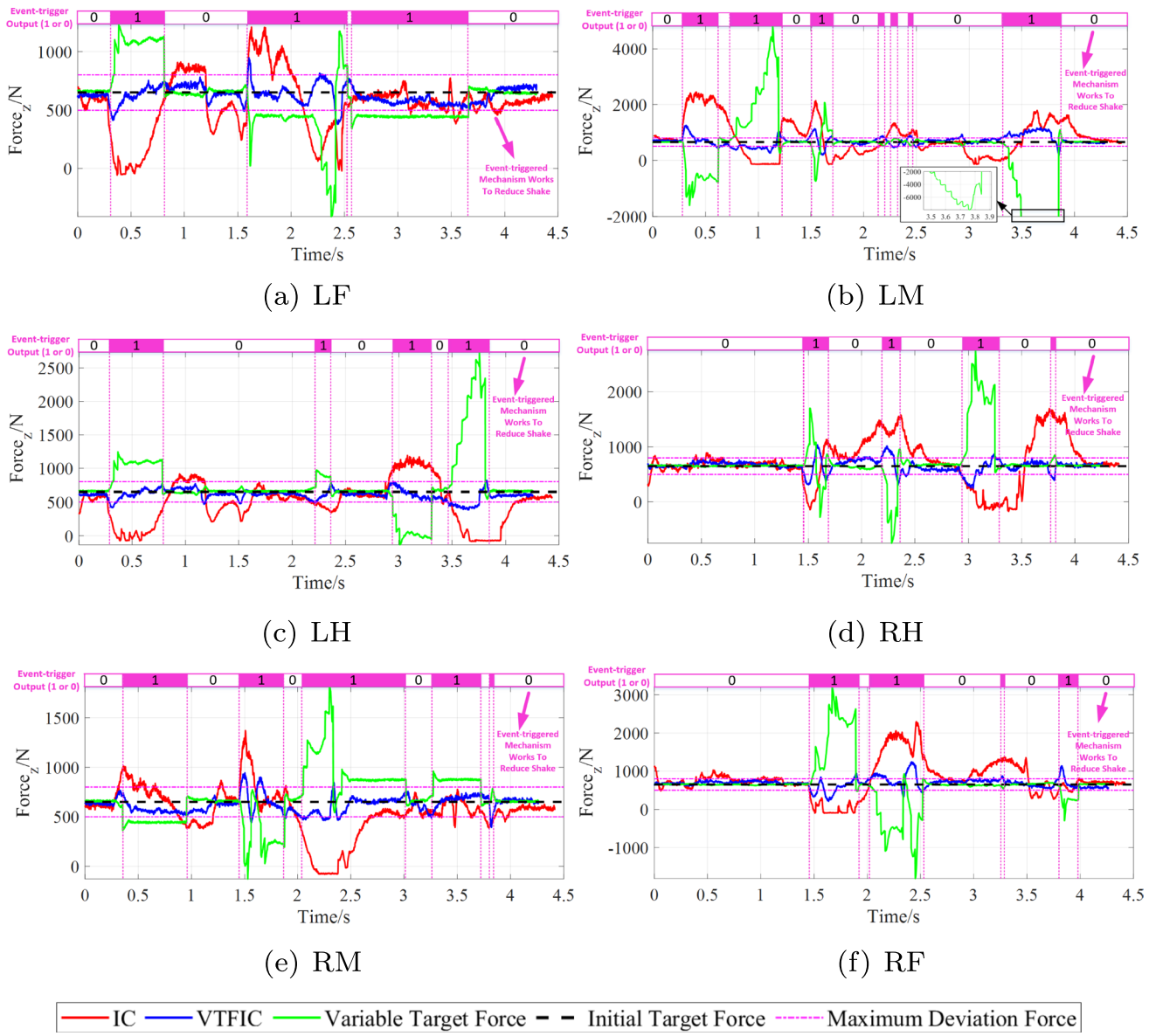

Fig. 22 Force of 1m/s speed under experiment of multiple slopes

illustrated. The stability and convergence of the algorithm are proved. In order to realize the dynamic force tracking better, the VTFIC includes the FDFE part by eliminating the disturbing force to reduce the steady-state error, and the FCAC part by using the power functional feed-forward path to accelerate the convergence speed. The simulation

Table 4 Deviation degree about attitude and force of multiple slopes experiment

dev	$\alpha(roll)/$	$\alpha(pitch)\circ$	*f/N*
IC	2.55	1.65	333.1
VTFIC	0.92	0.45	122.6

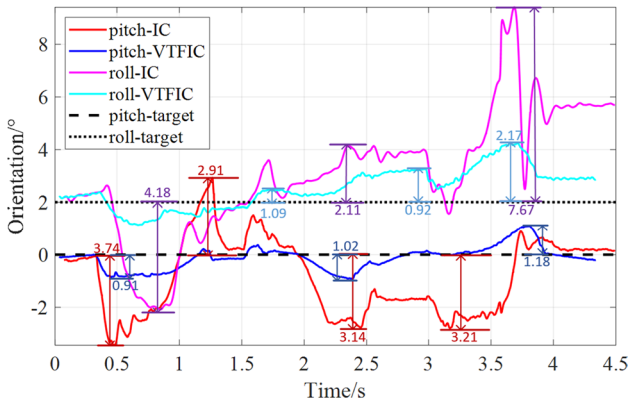

Fig. 23 Attitude of robot body under experiment of multiple slope

and experiment of the wheel-legged robot verify the force tracking effect under VTFIC, and compared with the effect under IC. The experimental results show that the desired foot-end force has better tracking effect, and the pitch angle and roll angle of the body have better stability under proposed method. The improvement of the dynamic stability of the robot can assist the robot to carry out the load work of rapid wheel movement in more environments, such as star exploration, disaster relief, etc. In the future research, the dynamic force of the robot parallel to the ground plane should be studied to reduce the slip and drift of the robot when it moves rapidly on the rough ground, so as to better ensure the stability of the body.

Fig. 24 Drive and walk on the outdoor environment

Author Contributions Junfeng Xue: Writing, Editing, Simulation, Experiment, Idea generation; Shoukun Wang: Supervision and Finalizing; Junzheng Wang: Reviewing and Supervision; Zhihua Chen: Writing, Editing;Experiment; All authors read and approved the final manuscript.

Funding This work was supported by the National Key Research and Development Program of China under Grant 2019YFC1511401, the National Natural Science Foundation of China under Grant 61103038, and the National Natural Science Foundation of China under Grant 61103060.

Data Availability The data that support the findings of this study are available from the corresponding author Prof. Zhihua Chen upon reasonable request.

Declarations

Conflicts of Interest No conflict of interest exists in the submission of this manuscript.

Consent to Participate All authors have participated in conception and design, or analysis and interpretation of the data; drafting the article or revising it critically for important intellectual content, and approval of the final version.

Consent to Publish The authors declare no interest conflict regarding the publication of this paper.

References

1. Chen, Z., Li, J., Wang, J., Wang, S., Zhao, J., Li, J.: Towards hybrid gait obstacle avoidance for a six wheel-legged robot with payload transportation. J. Intell. Robot. Syst. **102**(3), 1–21 (2021)
2. Chen, Z., Li, J., Wang, S., Wang, J., Ma, L.: Flexible gait transition for six wheel-legged robot with unstructured terrains. Robotics and Autonomous Systems p. 103989 (2022)
3. Huang, D., Yang, C., Pan, Y., Cheng, L.: Composite learning enhanced neural control for robot manipulator with output error constraints. IEEE Trans. Industr. Inf. **17**(1), 209–218 (2021)
4. Li, J., Dai, Y., Wang, J., Su, X., Ma, R.: Towards broad learning networks on unmanned mobile robot for semantic segmentation. In: 2022 IEEE International Conference on Robotics and Automation (ICRA), pp. 1–7. IEEE (2022)
5. Li, J., Wang, J., Peng, H., Hu, Y., Su, H.: Fuzzy-torque approximation-enhanced sliding mode control for lateral stability of mobile robot. IEEE Trans. Syst. Man Cybern. A Syst. **52**(4), 2491–2500 (2022)
6. Li, J., Wang, J., Peng, H., Zhang, L., Hu, Y., Su, H.: Neural fuzzy approximation enhanced autonomous tracking control of the wheel-legged robot under uncertain physical interaction. Neurocomputing **410**, 342–353 (2020)
7. Li, J., Wang, J., Wang, S., Yang, C.: Human-robot skill transmission for mobile robot via learning by demonstration. Neural Computing and Applications pp. 1–11 (2021). https://doi.org/10.1007/s00521-021-06449-x
8. Li, J., Zhang, X., Li, J., Liu, Y., Wang, J.: Building and optimization of 3d semantic map based on lidar and camera fusion. Neurocomputing **409**, 394–407 (2020)
9. Sartori, D., Quagliotti, F., Rutherford, M.J., Valavanis, K.P.: Implementation and testing of a backstepping controller autopilot for fixed-wing uavs. J. Intell. Robot. Syst. **76**(3), 505–525 (2014)
10. Wang, S., Chen, Z., Li, J., Wang, J., Li, J., Zhao, J.: Flexible motion framework of the six wheel-legged robot: experimental results. IEEE/ASME Transactions on Mechatronics (2021)
11. Yang, C., Huang, D., He, W., Cheng, L.: Neural control of robot manipulators with trajectory tracking constraints and input saturation. IEEE Trans. Neural Netw. Learn. Syst. **32**(9), 4231–4242 (2021)
12. Zeng, C., Chen, X., Wang, N., Yang, C.: Learning compliant robotic movements based on biomimetic motor adaptation. Robotics and Autonomous Systems **135**, 103,668 (2021)
13. Endo, G., Hirose, S.: Study on roller-walker–multi-mode steering control and self-contained locomotion. J. Robot. Soc. Japan **18**(8), 1159–1165 (2000)
14. Kim, Y.S., Jung, G.P., Kim, H., Cho, K.J., Chu, C.N.: Wheel transformer: A wheel-leg hybrid robot with passive transformable wheels. IEEE Trans. Robot. **30**(6), 1487–1498 (2014)
15. Tadakuma, K., Tadakuma, R., Maruyama, A., Rohmer, E., Nagatani, K., Yoshida, K., Ming, A., Shimojo, M., Higashimori, M., Kaneko, M.: Mechanical design of the wheel-leg hybrid mobile robot to realize a large wheel diameter. In: 2010 IEEE/RSJ International Conference on Intelligent Robots and Systems, pp. 3358–3365. IEEE (2010)
16. Grand, C., Benamar, F., Plumet, F.: Motion kinematics analysis of wheeled-legged rover over 3d surface with posture adaptation. Mech. Mach. Theory **45**(3), 477–495 (2010)
17. Li, X., Zhou, H., Feng, H., Zhang, S., Fu, Y.: Design and experiments of a novel hydraulic wheel-legged robot (wlr). In: 2018 IEEE/RSJ International Conference on Intelligent Robots and Systems (IROS), pp. 3292–3297. IEEE (2018)
18. Chen, Z., Wang, S., Wang, J., Xu, K., Lei, T., Zhang, H., Wang, X., Liu, D., Si, J.: Control strategy of stable walking for a hexapod wheel-legged robot. ISA Trans. **108**, 367–380 (2021)
19. Xue, J., Wang, S., Li, J., Wang, J., Zhang, J., Chen, Z.: Impedance-based foot-end torque vibration isolation control of parallel structure wheel-leg robot. The 2022 WRC Symposium on Advanced Robotics and Automation (WRC SARA) (2022)
20. Du, H., Gao, F.: Fault tolerance properties and motion planning of a six-legged robot with multiple faults. Robotica **35**(6), 1397–1414 (2017)
21. Jung, S., Hsia, T., Bonitz, R.: Force tracking impedance control of robot manipulators under unknown environment. IEEE Trans. Control Syst. Technol. **12**(3), 474–483 (2004). https://doi.org/10.1109/TCST.2004.824320
22. Kim, T., Kim, H.S., Kim, J.: Position-based impedance control for force tracking of a wall-cleaning unit. Int. J. Precis. Eng. Manuf. **17**(3), 323–329 (2016)
23. Kronander, K., Billard, A.: Stability considerations for variable impedance control. IEEE Trans. Robot. **32**(5), 1298–1305 (2016)
24. Chen, Z., Wang, S., Wang, J., Xu, K.: Attitude stability control for multi-agent six wheel-legged robot. IFAC-PapersOnLine **53**(2), 9636–9641 (2020)
25. Peng, H., Wang, J., Shen, W., Shi, D.: Cooperative attitude control for a wheel-legged robot. Peer-to-Peer Netw. Appl. **12**(6), 1741–1752 (2019)
26. Xin, Y., Chai, H., Li, Y., Rong, X., Li, B., Li, Y.: Speed and acceleration control for a two wheel-leg robot based on distributed dynamic model and whole-body control. IEEE Access **7**, 180,630–180,639 (2019)
27. Xu, K., Wang, S., Wang, X., Wang, J., Chen, Z., Liu, D.: High-flexibility locomotion and whole-torso control for a wheel-legged robot on challenging terrain*. In: 2020 IEEE International Conference on Robotics and Automation (ICRA), pp. 10,372–10,377 (2020)
28. Yue, B., Wang, S., Chen, Z., Xu, K., Wang, J.: Research on vibration isolation control of six wheel-legged robot based on

impedance control. In: 2020 39th Chinese Control Conference (CCC), pp. 3978–3983. IEEE (2020)
29. Huang, H., He, W., Wang, J., Zhang, L., Fu, Q.: An all servo-driven bird-like flapping-wing aerial robot capable of autonomous flight. IEEE/ASME Transactions on Mechatronics (2022)
30. Yu, X., He, W., Li, Q., Li, Y., Li, B.: Human-robot co-carrying using visual and force sensing. IEEE Trans. Ind. Electron. **68**(9), 8657–8666 (2020)
31. Yu, X., Li, B., He, W., Feng, Y., Cheng, L., Silvestre, C.: Adaptive-constrained impedance control for human-robot co-transportation. IEEE transactions on cybernetics (2021)
32. Sharifi, M., Behzadipour, S., Vossoughi, G.: Nonlinear model reference adaptive impedance control for human-robot interactions. Control. Eng. Pract. **32**, 9–27 (2014)
33. Duan, J., Gan, Y., Chen, M., Dai, X.: Adaptive variable impedance control for dynamic contact force tracking in uncertain environment. Robot. Auton. Syst. **102**, 54–65 (2018)
34. Xu, K., Wang, S., Yue, B., Wang, J., Peng, H., Liu, D., Chen, Z., Shi, M.: Adaptive impedance control with variable target stiffness for wheel-legged robot on complex unknown terrain. Mechatronics **69**, 102,388 (2020)
35. Kasaei, M., Abreu, M., Lau, N., Pereira, A., Reis, L.P.: Robust biped locomotion using deep reinforcement learning on top of an analytical control approach. Robotics and Autonomous Systems **146**, 103,900 (2021)
36. Vincent, I., Sun, Q.: A combined reactive and reinforcement learning controller for an autonomous tracked vehicle. Robot. Auton. Syst. **60**(4), 599–608 (2012)
37. Li, Z., Liu, J., Huang, Z., Peng, Y., Pu, H., Ding, L.: Adaptive impedance control of human-robot cooperation using reinforcement learning. IEEE Trans. Ind. Electron. **64**(10), 8013–8022 (2017). https://doi.org/10.1109/TIE.2017.2694391
38. Izadbakhsh, A., Khorashadizadeh, S., Ghandali, S.: Robust adaptive impedance control of robot manipulators using szász–mirakyan operator as universal approximator. ISA Transactions **106**, 1–11 (2020). https://doi.org/10.1016/j.isatra.2020.06.017.https://www.sciencedirect.com/science/article/pii/S0019057820302640
39. Brahmi, B., Driscoll, M., El Bojairami, I.K., Saad, M., Brahmi, A.: Novel adaptive impedance control for exoskeleton robot for rehabilitation using a nonlinear time-delay disturbance observer. ISA Transactions **108**, 381–392 (2021). https://doi.org/10.1016/j.isatra.2020.08.036.https://www.sciencedirect.com/science/article/pii/S0019057820303682
40. Roveda, L., Maskani, J., Franceschi, P., Abdi, A., Braghin, F., MolinariTosatti, L., Pedrocchi, N.: Model-based reinforcement learning variable impedance control for human-robot collaboration. Journal of Intelligent & Robotic Systems (2020)
41. Peng, H., Wang, J., Wang, S., Shen, W., Shi, D., Liu, D.: Coordinated motion control for a wheel-leg robot with speed consensus strategy. IEEE/ASME Trans. Mechatron. **25**(3), 1366–1376 (2020)
42. Zhihua, C., Shoukun, W., Kang, X., Junzheng, W., Jiangbo, Z., Shanshuai, N.: Research on high precision control of joint position servo system for hydraulic quadruped robot. In: 2019 Chinese Control Conference (CCC), pp. 755–760. IEEE (2019)
43. Hao, R., Wang, J., Zhao, J., Wang, S.: Observer-based robust control of 6-dof parallel electrical manipulator with fast friction estimation. IEEE Trans. Autom. Sci. Eng. **13**(3), 1399–1408 (2016). https://doi.org/10.1109/TASE.2015.2427743
44. Shi, D., Xue, J., Zhao, L., Wang, J., Huang, Y.: Event-triggered active disturbance rejection control of dc torque motors. IEEE/ASME Trans. Mechatron. **22**(5), 2277–2287 (2017)

Junfeng Xue received the B.S. degree in measurement and control technology and instruments from Beijing university of technology in China in 2021. He is currently a M.S. student at School of Automation, Beijing Institute of Technology, China. His research interests include robot control, wheeled motion control, and vibration isolation control of robot.

Shoukun Wang received the B.S., M.S., and Ph.D. degree in department of automation, from Beijing Institute of Technology, Beijing, China, in 1999,2002,2004 respectively. He has entered in Department of Electronics and Computer Engineering, the Purdue University, West Lafayette, USA as a visiting scholar. He has been teaching at the School of Automation, Beijing Institute of Technology, since 2004. His research interests include sensor, measurement, and electro-hydraulic control. He has participated in over 30 scientific research projects since 2001, which mainly belong to measurement and servo control. He has also served as the leader in some of these works. His main work focused on Electrical-hydraulic control algorithm, robot locomotion control, and visual servo.

Junzheng Wang received the Ph.D. degree in control science and engineering from the Beijing Institute of Technology, Beijing, China, in 1994. He is the Deputy Director with the State Key Laboratory of Intelligent Control and Decision of Complex Systems, the director of the Key Laboratory of Servo Motion System Drive and Control, and the Dean of the Graduate School of Beijing Institute of Technology, where he is a Professor and a Ph.D. Supervisor. His current research interests include motion control, static and dynamic performance testing of electric and electric hydraulic servo system, and dynamic target detection and tracking based on image technology. Prof. Wang is a senior member of the Chinese Mechanical Engineering Society and the Chinese Society for Measurement. He received the Second Award from the National Scientific and Technological Progress (No.1) in 2011.

Zhihua Chen received the M.Sc. degree in mechatronics engineering at Beijing Information Science and Technology University, Beijing, China, in 2018. He received the Ph.D. degree of control science and engineering as a member of State Key Laboratory of Intelligent Control and Decision of Complex Systems, Beijing Institute of Technology, China, in 2022. He is currently a teacher at School of Information Engineering, Nanchang Hangkong University, China. His current research interests are robot legged motion control, wheel-legged motion planning, obstacle avoidance. He has served as a reviewer for some scientific journals, such as IEEE Transactions on Industrial Electronics, IEEE/ASME Transactions on Mechatronics, ISA Transactions, ASME Journal of Dynamic Systems, Measurement and Control, and so on.